# Friction and Surface Dynamics of Polymers on the Nanoscale by AFM

Holger Schönherr (✉) · Ewa Tocha · G. Julius Vancso (✉)

MESA+ Institute for Nanotechnology and Faculty of Science and Technology,
University of Twente, Department of Materials Science and Technology of Polymers,
P.O. Box 217, 7500 AE Enschede, The Netherlands
*h.schonherr@utwente.nl, g.j.vancso@utwente.nl*

**Abstract** In this article the measurement and understanding of friction forces and surface dynamics of polymers on the one hand and the importance of molecular relaxation processes and viscoelasticity in polymers for advanced micro- and nanoscale applications on the other hand are discussed. Particular attention is paid to the nanoscale (surface)

analysis by scanned probe microscopic approaches, including atomic force microscopy (AFM), as a means to assess molecular relaxation processes that operate at a given temperature. Established AFM approaches, including lateral force and force modulation microscopy, are introduced and more recently developed techniques, such as torsional resonant modes, are briefly sketched. On the basis of the discussion of the techniques to measure friction and to probe surface dynamics of polymers on the nanoscale, illustrative examples are reviewed. The examples discussed address in particular the determination of values of the glass transition temperature ($T_g$) and the difference of $T_g$ assessed in the bulk vs. at the free surface of polymers. Confinement and thin film effects on $T_g$, but also on sub-$T_g$ transitions and chain dynamics, are treated in detail. Finally, the mapping of multiphase systems and anisotropic friction receive attention.

**Keywords** AFM · Confinement effects · Friction · Glass transition temperature · Nanotribology · Polymer viscoelasticity · Thin film effects

**Abbreviations**

| | |
|---|---|
| AFM | Atomic force microscopy |
| FFM | Friction force microscopy |
| SM-FM | Shear modulation force microscopy |
| SVM | Scanning viscoelasticity microscopy |
| SLAM | Scanning local acceleration microscopy |
| TR | Torsional resonance |
| LFM | Lateral force microscopy |
| CFM | Chemical force microscopy |
| HFM | Heterodyne force microscopy |
| $f$–$d$ | Force-displacement |
| $T_g$ | Glass transition temperature |
| MEMS | Microelectromechanical systems |
| NEMS | Nanoelectromechanical systems |
| SFA | Surface forces apparatus |
| JKR model | Johnson, Kendall and Roberts model |
| DMT model | Derjaguin, Muller, Toporov model |
| PMMA | Poly(methyl methacrylate) |
| PMA | Poly(methyl acrylate) |
| PnBMA | Poly($n$-butyl methacrylate) |
| PtBuA | Poly($tert$-butyl methacrylate) |
| PTFE | Poly(tetrafluoroethylene) |
| PS | Polystyrene |
| PI | Polyisoprene |
| PE | Polyethylene |
| PP | Polypropylene |
| EP | Ethylene-propylene |
| PES/SAN | Poly(ether sulfone)/polyethersulfone/poly(acrylonitrile-$co$-styrene) |
| PVOH | Poly(vinyl alcohol) |
| PVP | Poly(vinyl pyridine) |
| OTS | Octadecyltrichlorosilane |
| PVME | Poly(vinyl methylether) |

# 1
# Introduction

Friction and (surface) dynamics of polymers play an important role not only in advanced applications related to adhesives, lubricants and protective coatings and in everyday life (e.g. the low adhesion and low friction properties of poly(tetrafluoroethylene), PTFE, coatings), but following the accelerating drive towards nanometer scale technology and devices, these phenomena may become limiting factors in various applications. A closer look at the state of the art in this area shows that there is, in particular in the area of tribology, despite decades of research, a wide gap in terms of length and time scales between theory (modeling), nanoscale and micro-/macroscale experimental work [1, 2].

Clearly, the mastering of the theoretical treatment and understanding of the chain dynamics of polymers in the bulk, as developed by the pioneering work of Williams, Landel, Ferry and many others [3], had an enormous impact on polymer science on the one hand and via the research and development in the polymer industry on high tech and low tech applications that are today commonplace on the other hand. With shrinking dimensions, for instance in coatings in data storage devices [4] or in fabrication processes like photoresist technology-based lithography [5], substrate and interface effects, confinement effects and thereby affected chain dynamics alter the known bulk behavior of polymers [6]. Effects include, among others, altered transport properties [7] as well as crystallization [8] and dewetting kinetics [9]. Most strikingly this is illustrated in the pronounced effect of the ultrathin film architecture (surface/interface chemistry, film thickness) of substrate-supported polymer films on the glass transition temperature ($T_g$) and polymer chain dynamics [10–12]. Altered $T_g$'s of up to 50 °C have been reported [10–13].

The molecular origin for friction in polymers is, as will be pointed out below, directly linked to the molecular relaxation processes that operate at a given temperature. Near $T_g$ friction in polymer melts shows highly cooperative dissipation phenomena, known as heterogeneous dynamics of glass formers. The associated critical length scale, over which collective molecular motion occurs, is called the size of a cooperatively rearranging region. This length scale ranges in the bulk from several monomeric segments to several molecules [14]. Such localized effects mandate the study of the underlying principles and the determination of the length scales by high-resolution techniques, i.e. by techniques that operate at the corresponding length scale.

In more general terms, in the understanding of friction, despite decade-long efforts, a gap can be identified between molecular or atomistic models on the one hand [15], and continuum (e.g. contact mechanics) approaches [17] that describe the deformation between elastic single asperities on the other hand [1]. Consequently, the understanding of fundamental aspects of friction and the mechanisms of energy dissipation remains limited on

a first-principles level. Multi-level experiments (from micrometer to nanometer scale) are clearly required to advance the understanding of tribology. The goal of the multi-level experiments is to determine the mechanism of friction, which is partly based on the atomic and molecular scale phenomena at the sliding interface, and to correlate the corresponding processes to the macroscopic scale frictional behavior. The necessary bridge between micro- and nanotribology, as well as atomistic [15, 16] and continuum models [17, 18] has not yet been addressed convincingly. Both experimental (tribology) and theoretical (simulations) approaches suffered until recently from limitations that prevented a unified understanding.

On the basis of atomic force microscopy (AFM) [19], as one of the more prominent members of the family of proximal probe techniques, a number of highly interesting approaches has been developed in the last ∼10 years to start to *quantitatively* address friction and in particular surface dynamics of polymers at the true nanoscale [1, 2, 20]. In general, AFM is attractive for studies at the fundamental level of single asperities, since the method is suitable for the detection of friction forces of nanometer scale contacts of real surfaces with high spatial resolution under pressures of up to several GPa [21]. With these new approaches at hand, one of the main challenges of modern tribology can be tackled, namely to develop a fundamental understanding of nanoscale friction. For polymers additional challenges arise due to the complexities of the time–temperature superposition principle [22] and the fact that the instruments utilized in nano- and microtribology until recently operated on different time and length scale regimes. In addition, polymers can easily be deformed plastically, thus giving rise to altered contact areas and pressures, as well as friction mechanisms other than interfacial friction.

The ability of controlling friction (of polymers), once achieved, will be highly advantageous in new technological developments, such as magnetic storage devices [23, 24], and applications, such as in microelectromechanical systems (MEMS) and nanoelectromechanical systems (NEMS) [25], biosystems [26], and many others. In this review we aim at a concise treatment of friction and its relation to polymer (chain) surface dynamics. On the basis of a rudimentary introduction of polymer viscoelasticity and (nano)tribology, we review the recent progress in the use of AFM technology to explore friction of polymers on the nanoscale. In this review we rely on work published in the literature, as well as on the work performed in our laboratory to provide a broad overview of the topic both for the expert as well as the non-expert readers who want to enter this exciting field.

## 1.1
## Polymer Dynamics and Viscoelasticity

Amorphous polymers show a distinct change in mechanical properties when passing through the glass–rubber transition at the glass transition tempera-

ture ($T_g$) [27, 28]. As a result of frozen chain motions, the Young's modulus is ~3 orders of magnitude higher at temperatures below $T_g$ than for temperatures above $T_g$. In addition, amorphous polymers deform in a first approximation elastically below $T_g$, while polymer melts at temperatures above $T_g$ are best described as viscoelastic non-Newtonian fluids. Even below $T_g$ polymers may show relaxation phenomena, such as the slow recovery after the application of a temporary stress, that are attributed to molecular scale motions. These include the rotation of pending side groups or the crankshaft motion of the polymer backbone. In particular in the light of polymer ageing, these processes are of great importance.

In addition to temperature, all these phenomena depend, as will be briefly alluded to below on the rate (frequency) of the experiment, e.g. the rate at which the stress is applied. For a dynamic-mechanical experiment, we can define the loss tangent $\tan(\delta)$ as the ratio of the dynamic loss modulus $E'$ and the dynamic storage modulus $E''$ [29]:

$$\tan(\delta) = \frac{E''}{E'} . \tag{1}$$

The relationship of $\tan(\delta)$ vs. frequency generally displays several broad peaks corresponding to different classes of molecular relaxations labeled $\alpha, \beta, \gamma$ and $\delta$. These relaxation processes are ascribed to the glass–rubber transition and different rotations of side groups, respectively (vide infra). As mentioned, dramatic changes in various material properties are associated with this transition.

The variation of rate (time) and temperature causes similar effects in polymer relaxation processes. For viscoelastic properties the interplay between relaxation time and temperature is well-known [30–33]. The so-called time–temperature superposition principle states that the same molecular relaxation requires longer time at lower temperatures. For instance, a polymer, which displays rubbery characteristics under a given set of testing conditions, can be induced to show glassy behavior by either reducing the temperature (to below $T_g$) or by increasing the testing rate (or frequency). According to the time–temperature superposition principle (higher $T \Leftrightarrow$ lower frequency), the $\tan(\delta)$ vs. frequency relation can be reduced to a master curve at an arbitrary chosen reference temperature $T_o$, by multiplying the velocity (or frequency) data with the Williams–Landel–Ferry (WLF) shift factor $a_T$ [22]. The Arrhenius relationship

$$\ln a_T = \frac{E_a}{R} \left( \frac{1}{T} - \frac{1}{T_o} \right) \tag{2}$$

between the shift factor $a_T$ and the temperature $T$, and the activation energy $E_a$, is commonly used to analyze relaxation phenomena below $T_g$. The activation energies represent the potential barrier that is continuously overcome, e.g. for the rotation of dipolar moieties in macromolecules.

For instance, the relaxation processes in bulk poly(methyl methacrylate) (PMMA) are well characterized using a variety of techniques, including dielectric [34, 35] and dynamic mechanical analyses [36–38], NMR spectroscopy [39], positron annihilation [40], and fluorescence spectroscopy [38]. In PMMA the highest relaxation temperature, the $\alpha$ relaxation, is the glass transition temperature ($T_g$ = 95–110 °C, $E_a^\alpha$ = 334–460 kJ mol$^{-1}$) [29] and is ascribed to long-range conformational changes of the polymer backbone (see Fig. 1). The secondary $\beta, \gamma$, and $\delta$ relaxations are attributed to the side chain motions of the ester group and rotations of the methyl groups attached to the main chain and side chain, with characteristic relaxation temperatures $T_\beta$ = 10–40 °C, $T_\gamma$ = –100–170 °C, and $T_\delta$ = –180 °C, and activation energies $E_a^\beta$ = 71–96 kJ mol$^{-1}$, $E_a^\gamma$ = 10–29 kJ mol$^{-1}$, $E_a^\delta$ = 3 kJ mol$^{-1}$, respectively [29, 38, 41].
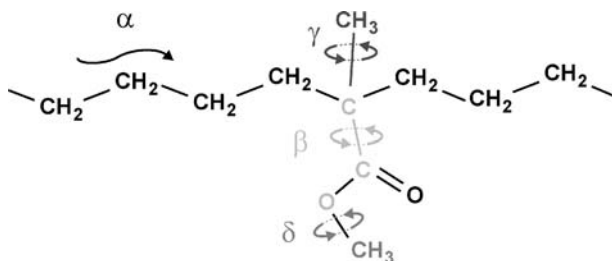


**Fig. 1** Schematic of the relaxations in PMMA

In general, the dependence of polymer relaxations on various parameters can be schematically captured in the form of tan($\delta$)–frequency or tan($\delta$)–temperature diagrams (Fig. 2). In the tan($\delta$) vs. frequency relation, the bell-shape curve characteristic for a relaxation with maximum at $f_o$ (relaxation frequency) is shifted to lower frequency values for increasing pressure. By contrast, increasing the temperature results in a shift to higher frequency
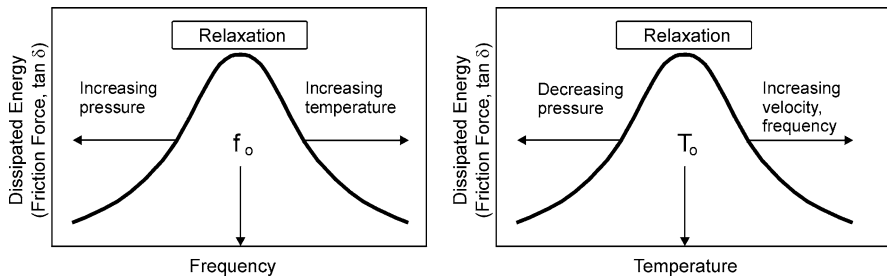


**Fig. 2** Schematic diagrams of a relaxation probed in a friction force–frequency (*left*) and a friction force–temperature experiment (*right*) of a polymer

values. As will be discussed in Sect. 3.2 in detail, dynamic friction of polymers has a large contribution from internal viscoelastic dissipation. Hence plots of the friction force, determined e.g. by AFM, vs. $f_o$ are qualitatively similar to plots of tan $\delta$ vs. $f_o$.

## 1.2
## Static and Dynamic Friction Force, Single vs. Multi Asperity Contacts

Friction forces and (surface) dynamics of polymers are intimately related, as already alluded to above. By measuring, for instance, dynamic friction forces under well-controlled conditions, the dynamics of a given polymer can be directly probed at the free surface of a sample specimen. Before discussing the proximal probe techniques and approaches that have been applied to the study of friction and surface dynamics of polymers at the nanoscale, some fundamental aspects of (nano)tribology will be briefly reviewed.

When a lateral force, or shear stress, is applied to two surfaces in adhesive contact, the surfaces initially remain "pinned" to each other until some critical shear force is reached. At this point, the surfaces begin to slide past each other either smoothly or in jerks. The friction force needed to initiate sliding from the rest position is known as the *static friction force*, denoted by $F_s$ (see Fig. 3). The force needed to maintain smooth sliding is referred to as the *kinetic* or *dynamic friction force*, denoted by $F_k$ or $F_f$. In general, $F_s > F_k$ [42]. Two sliding surfaces may also move in regular jerks, known as "stick-slip" sliding, which is discussed in more detail in Sect. 3.4. The friction force between two bodies in the absence of lubrication is often called *dry friction*.

In the most common situation *normal friction* (kinetic friction accompanied by wear and/or plastic deformation) takes place when two rough surfaces slide with respect to each other. The surface asperities may deform elastically or plastically. When a strong force is applied to the surfaces, damage (or wear) of the shearing substrates occurs. Under certain conditions (low load, completely elastic interactions, smooth tip shape, atomically flat substrate, unreactive surfaces, etc.) a single-asperity contact may be formed and wear-less friction can be observed. This situation is often referred to as *interfacial* or *boundary friction* [43]. In this regime it has been observed that



**Fig. 3** **a** The friction force needed to initiate sliding from rest is known as the static friction force, denoted by $F_s$. **b** The force needed to maintain smooth sliding is referred to as the kinetic or dynamic friction force, denoted by $F_k$ or $F_f$. $v$ stands for velocity

friction is proportional to the contact area. This type of friction can be probed using the surface forces apparatus (SFA) or by AFM.[1]

A general form of the normal friction force (also called lateral force) is given by [1]:

$$F_f = \mu F_N = \mu(L + A),$$                                                          (3)

where $\mu$ is the friction coefficient and $F_N$ denotes the *normal force*, which is calculated as the sum of externally applied load $L$ and the contribution from *adhesion forces* or *adhesion A* (the maximum force needed to separate two bodies).

On the basis of various studies by Amontons and Coulomb, three laws of friction have been formulated [1]:

1. The friction force is independent of the apparent area of contact.
2. The friction force ($F_f$) is proportional to the applied load ($L$): $F_f = \mu L$. The ratio $L/F_f$ is called coefficient of friction $\mu$. Its value is usually larger for static friction than for kinetic friction ($\mu_s > \mu_k$).
3. Kinetic friction is independent of the velocity.

These three macroscopic phenomenological laws of friction are still not fully understood in terms of the corresponding fundamental microscopic processes. However, these laws apply surprisingly well on the macroscopic scale for dry friction.

## 1.2.1
## Multiple and Single Asperity Tribology

The modern study of friction started in the 1950s, when Bowden and Tabor presented a simple model of friction on the micrometer scale [44]. They found that friction force, although independent of apparent microscopic contact area, is in fact proportional to the true contact area ($A_R$). Surfaces are rough on the microscopic scale, hence the microscopic irregularities of the surfaces touch and push into one another (Fig. 4). The real area of contact is therefore a few orders of magnitude smaller than the apparent area of contact. In the Bowden and Tabor model, the friction force between two unlubricated (dry) surfaces arises from two main factors (Eq. 4). The first, and usually the most important factor is the interaction between the asperities of the contacting surfaces. It is assumed that this part of the friction force is proportional to both the real area of contact $A_R$ and the interfacial shear strength $\tau^*$. The second factor, called the deformation term $D$, arises from

---

[1] SFA and AFM are among the most prominent instruments for performing micro- and nanotribological studies. While the SFA is limited to mica as a substrate and affords atomic resolution only in the vertical direction and has limited lateral resolution (several micrometers), AFM is suitable to detect friction forces with atomic resolution in all three dimensions of nanometer-scale contacts of real surfaces under pressures of several GPa.
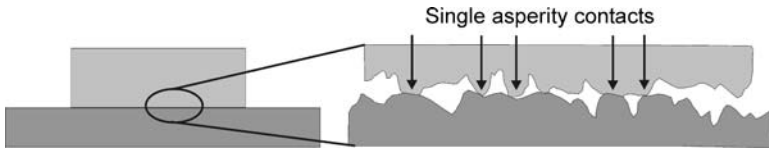
**Fig. 4** Surfaces are rough on the microscopic scale. The irregularities of the surfaces touch and push into one another. The real area of contact is a few orders of magnitude smaller than the apparent area of contact

the ploughing, grooving or cracking of one surface by asperities on the other surface.

$$F_f = \tau^* A_R + D \,. \tag{4}$$

Since the friction force is proportional to the real area of contact, as is adhesion (see Sect. 2.3), and since the energy loss in the friction mechanism is ascribed to plastic deformation of the asperities, the model is often called *adhesion model* or *plastic junction model* [44].

For purely plastic deformation, the area of contact $A_R$ is proportional to the load (which simplifies Eq. 4 to the second law by Amontons)[2]. However, totally plastic deformation during sliding provokes huge damage in a short time, which is usually not observed. Thus, elastic processes must play an important role in friction processes and other dissipation mechanisms must exist, which do not change the structure of the surfaces in contact [44].

Different length scales are relevant for microscopic experiments. The surface roughness will determine the size of the asperities. The smallest asperities are plastically deformed at very low loads, whereas larger asperities are still in the elastic regime (interfacial friction). On the micrometer scale the friction force has contributions from different phenomena, such as wear-less friction, plastic deformation of asperities, lateral forces to move debris particles, viscous forces and ploughing terms [1]. To understand the behavior of such a complex contact, it is hence desirable to learn about the properties of single asperity contacts under conditions of interfacial friction. In this case, the friction force was found to be proportional to the real area of contact, hence in good agreement with the Bowden and Tabor model. As will be shown below, a non-linear friction force–load dependence is expected for single asperity contacts, which is in contradiction to Amontons' friction law.

In macroscopic contacts, the interface consists of many micrometer and submicrometer size asperities, where real contact occurs. Contact continuum mechanics describe the elastic deformation of single asperities. All theories described below are based on the following assumptions: the deformations

---

[2] If the deformation is totally plastic, the asperities are compressed until the pressure becomes equal to a certain yield pressure $p^*$, which is usually smaller than the yield pressure of the bulk material.

are purely elastic, the contacting materials are elastically isotropic, Young's modulus and Poisson's ratio are not load dependent, the atomic structure is not considered, and the contact radius $a$ is small compared to the radius $R$ of the sphere.

## 1.2.2
## Hertz Model

The Hertz theory [45] assumes that no attractive forces act between the two materials. For a sphere–sphere contact, the contact area $A_R$ depends on load $L$:

$$A_R = \pi \left( \frac{R \cdot L}{K} \right)^{\frac{2}{3}} \tag{5}$$

$$\frac{1}{R} \equiv \frac{1}{R_1} + \frac{1}{R_2} \tag{6}$$

$$K \equiv \frac{4}{3} \left( \frac{1 - \nu_1^2}{E_1} + \frac{1 - \nu_2^2}{E_2} \right)^{-1}, \tag{7}$$

where $R$ is the composite radius and $R_1$, $R_2$ are the radii of curvature of the lower and upper body, respectively, $K$ is the reduced elastic modulus, $E_1$, $E_2$ and $\nu_1$, $\nu_2$ are the Young's moduli and Poisson's ratios for the lower and upper body, respectively (Fig. 5).
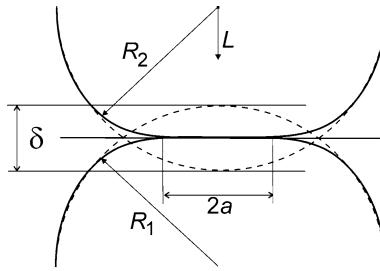


**Fig. 5** Geometry of a contact between two elastic spheres ($R_1$ and $R_2$) under applied load $L$ for the Hertz theory; $a$ denotes the contact radius, $\delta$ is the indentation depth

## 1.2.3
## Johnson, Kendall and Roberts (JKR) Model

The JKR model [46, 47] is the extension of the Hertz model, in which the work of adhesion $\gamma$ is taken into account ($\gamma$ is defined as the energy per unit area to separate two flat surfaces in vacuum from contact to infinity). It assumes that the adhesive forces are confined to the inside of the contact area. The contact

area is described by:

$$A(L) = \pi \left(\frac{R}{K}\right)^{\frac{2}{3}} \left(L + 3\pi\gamma R + \sqrt{6\pi\gamma RL + (3\pi\gamma R)^2}\right)^{2/3} . \tag{8}$$

Even at zero applied load there is a finite contact area of $A_R(0) = \pi(6\pi\gamma R^2/K)^{2/3}$. Hence, load has to be applied to break the contact. In the limit of work of adhesion equal to zero ($\gamma \rightarrow 0$) and also for large forces compared to $\gamma R$, the JKR result coincides asymptotically with the Hertzian result. The derivative of $R_A$ with respect to load yields the minimum for the contact area (area at pull-off, see Sect. 2.3.1 for AFM pull-off force), which can be transformed to equation:

$$F_{\text{Pull-off}}^{\text{JKR}} = -\frac{3}{2}\pi R W_{12} . \tag{9}$$

The work of adhesion $\gamma = W_{12}$ can be expressed as a function of the surface energies of the tip $\gamma_1$, the sample $\gamma_2$, and the corresponding interfacial energy $\gamma_{12}$:

$$W_{12} = \gamma_1 + \gamma_2 - \gamma_{12} . \tag{10}$$

The JKR model can be applied when the surface forces are short range in comparison to the elastic deformations they cause (i.e. compliant materials, strong adhesion force, large tip radii).

### 1.2.4
### Derjaguin, Muller, Toporov (DMT) Model

The DMT model includes adhesion outside the contact area by considering long-range attractive forces of van der Waals type [48–51]. Maugis provided an analytical solution for the model [52]. In this case, the real area of contact $A_R$ varies with load $L$ in a simple fashion:

$$A_R = \pi \left[\frac{R}{K}(L + 2\pi R\gamma)\right]^{2/3} . \tag{11}$$

The pull-off force is given by:

$$F_{\text{Pull-off}}^{\text{DMT}} = -2\pi R W_{12} . \tag{12}$$

The JKR and DMT models apply for two extreme cases: for compliant materials with large, short-range attractive forces and for stiff materials with small, long-range attractive forces, respectively. The parameter $\lambda$ is used to determine which of the two models is most appropriate.

$$\lambda = \left(\frac{9RW_{12}^2}{4\pi K^2 z_0^3}\right)^{1/3} , \tag{13}$$

where $z_o$ is the equilibrium separation between the contacting surfaces. If $\lambda > 5$, the JKR theory should be valid, while for $\lambda < 0.1$ the DMT theory should describe the relation between $A_R$ and $L$ [17, 53]. The most frequently used description covering the JKR–DMT transition regime is the Maugis–Dugdale (MD) theory [52]. The model is relatively difficult to use because it is presented in two coupled analytical equations that must be solved numerically through iteration.

Recently, Carpick, Ogletree and Salmeron [17], as well as Schwarz [54] proposed a general analytical model for the elastic deformation of an adhesive contact in the intermediate regime between JKR and DMT limits as an alternative.

The application of the elastic contact continuum models for viscoelastic materials is limited. For instance, the models can be used only for materials that possess a glass transition temperature well above ambient temperature. For a viscoelastic material the size of the contact zone depends on the loading history. Several attempts have been made to modify the JKR theory with some relaxation functions. A combination model of classical JKR theory with a fracture mechanics model of crack initiation and growth in linear viscoelastic materials has been proposed by Johnson [55, 56]. The major assumption of the model is that viscoelastic effects are limited to the periphery of the contact. Longer-range creep effects are ignored. Hui et al. extended the JKR theory for the contact radius which is a non-decreasing function of time (describing the bonding process). The presented models are complex and often necessitate the use of numerical calculations [57–59].

## 1.2.5
## The Greenwood and Williamson Model of Multiasperity Contact

Realistic surface interactions are influenced not only by the nominal apparent or contact areas $A_n$, but also by the individual asperity/roughness interactions. Greenwood and Williamson modeled surface roughness using a statistical model, where the roughness of two approaching surfaces is combined into an infinitely smooth surface and a surface with spherically shaped asperities having a uniform mean radius $R$ and following a Gaussian height distribution. A linear dependence between the real contact area and the applied load was obtained independently of the mode of deformation of the asperities (i.e. whether it is elastic, plastic or something in-between) or the shape of asperities [60–62]. In this case, the Greenwood model leads to Amontons' law, as well as to the plastic junction model [44].

## 2
## Techniques to Measure Friction and to Probe Surface Dynamics of Polymers on the Nanoscale and Illustrative Examples

As mentioned in the introduction, the length scales over which energy is dissipated can be directly linked to relaxation processes in the polymer and in the case of the glass transition to the corresponding clustering processes. Hence it is not surprising that a large number of proximal probe techniques has been developed to measure friction and to probe surface dynamics of polymers on the nanoscale.

We focus in the following on a brief description of the rudimentary aspects of the most commonly applied AFM-related techniques, in particular lateral force microscopy (friction force microscopy). In addition, all relevant techniques will be introduced that have been applied to acquire the data reviewed and discussed in Sect. 3. It is important to note that different techniques rely on the detection and quantification of different physicochemical parameters. In addition, among these techniques other factors or parameters may or may not have been maintained constant. Sometimes even identical techniques were applied in different ways. Thus, even though various authors report the same "quantity", e.g., a surface glass transition temperature, for nominally identical polymers, the absolute numbers, but also the trends observed may differ widely.

### 2.1
### Friction Force Microscopy

One of the very prominent techniques to measure friction on the nanoscale is the so-called friction force microscopy (FFM) or, more generally, lateral force microscopy (LFM) [63, 64]. This technique is a contact mode atomic force microscopy (AFM) technique, in which both normal and lateral forces are measured simultaneously. In contact mode AFM a sharp tip (with a typical radius of 10–100 nm and a typical probe material of Si and $Si_3N_4$) mounted to the end of a flexible cantilever (with a normal spring constant of $k_N = 0.01–1\,N\,m^{-1}$) is brought into contact with the surface. While scanning either by the tip or by the sample (Fig. 6), forces acting between atoms of the AFM tip and atoms of the sample surface will result in a measurable deflection of the cantilever. The cantilever bends vertically (i.e. towards or away from the sample) in response to attractive and/or repulsive forces acting on the tip (see Sect. 2.3). Using, for instance, a feedback loop to maintain a constant cantilever deflection, while scanning the sample surface, a topographic image of the surface can be obtained by plotting the feedback signal vs. tip position.

When the sample is scanned perpendicular to the main cantilever axis in the constant force mode, lateral forces acting on the tip result in twist-
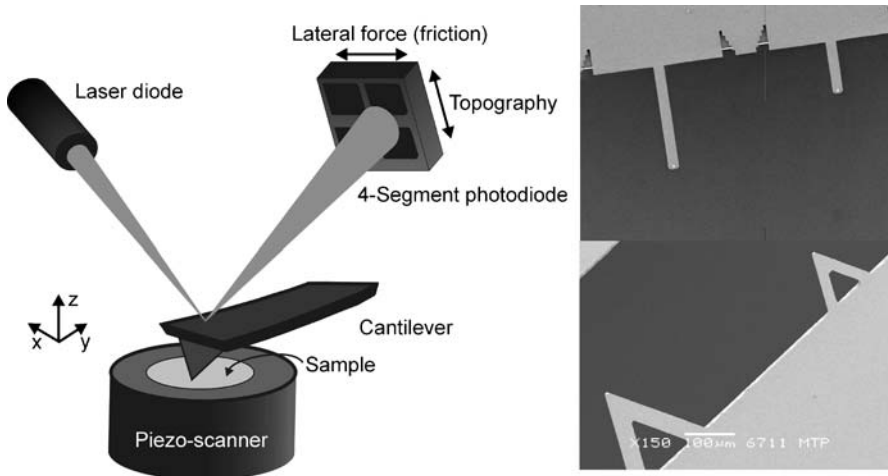
**Fig. 6** *Left*: Schematic diagram of contact mode AFM; *right*: SEM images of single beam and V-shaped cantilevers

ing of the cantilever [65]. The magnitude of the cantilever torsion (lateral deflection) is proportional to the friction forces of the tip–sample contact. Simultaneous measurements of the normal and lateral deflections can be performed using several techniques, including a four-segment photodiode (also called optical beam deflection method) [66]. The optical deflection method as the most frequently utilized technique to monitor forces in AFM is based on detection of laser beam position reflected from the back of the cantilever into a position sensitive four-segment photodiode. The voltages measured on the four segment photodiode in normal and lateral direction are defined as the difference voltage between top and bottom photodiode output: $\Delta U_{N} = ((A + B) - (C + D))/(A + B + C + D)$ and difference voltage between left and right photodiode output: $\Delta U_{L} = ((A + C) - (B + D))/(A + B + C + D)$, and are labeled *difference normal signal* and *difference friction signal*, respectively. The method, in fact, measures the deflection angles and bending angles of the cantilever, which are linearly proportional to the cantilever deflections (normal and lateral, respectively) for small angles.

Lateral forces acting on the cantilever tip in a direction perpendicular to the cantilever main axis will twist the cantilever. Typical AFM friction measurements are recorded in the form of friction loops, as shown in Fig. 7. In the friction loop, the difference friction signal (also called friction signal) is plotted against the trace (forward scan) and retrace (backward scan) lateral sample displacement. At the beginning of each trace and retrace, the sample remains in static contact until the shear force increases and overcomes the static friction force. The signal changes sign for the retrace with respect to the trace scan. For a given load (normal force), the friction force can be deter-
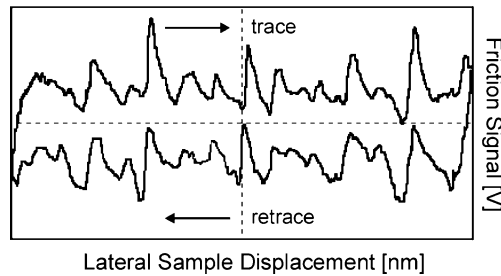
**Fig. 7** Typical friction loop in which the differential photodiode output signal for cantilever torsion is recorded for forward (trace) and backwards (retrace) scans along the same scan line

mined as one half of the difference between the corresponding friction signals for trace and retrace scans.

The friction loop may contain information originating from topographic features [67]. Most of this topographic component (i.e. the local slope of the sample surface)[3] is removed from the difference friction signals by subtracting the data for trace and retrace scan directions. However, thermal drift and hysteresis in the lateral scan system may prevent an exact match of trace and retrace data. For quantitative analyses a correction (off-set) of trace and retrace data may be required. In addition, a fundamental requirement for quantitative LFM are symmetric, i.e. spherical tip apex shapes. The friction force can also be determined from trace and retrace lateral force images, as the difference image (also called friction map). By creating histograms of the force maps, the friction forces can be quantified [30].

In order to obtain quantitative data from force microscopy, a reliable and accurate force calibration must be performed [21]. This requires, both the calibration of the normal and lateral force constants of the cantilevers and of the photodiode sensitivity [68]. The normal and lateral forces acting on the cantilever can be expressed as:

$$F_N = k_N S_N \Delta U_N \tag{14}$$

$$F_L = k_L S_L \Delta U_L = \alpha \cdot \Delta U_L , \tag{15}$$

where $\alpha$ denotes the lateral calibration factor, which transforms the measured lateral difference signal [V] into friction force [nN]. As the values of $S_N$ and $S_L$ are very sensitive to the position of the laser beam on the cantilever apex [68–70], and the corresponding spot shape [71], the sensitivities must be determined for each cantilever and also for each position of the laser beam on the cantilever [72, 73].

---

[3] The reaction force from a tilted surface (with respect to the horizontal) will impose a lateral force on the tip, even in a case of zero friction.

The force constants of *single beam* cantilevers (normal spring constant $k_N$, torsional spring constant $k_\varphi$, and lateral spring constant $k_L$) can be calculated, assuming levers of constant thickness, based on measured cantilever dimensions, from continuum elasticity mechanics of isotropic solids [74–76]:

$$k_N = \frac{Ewt^3}{4l^3} \tag{16}$$

$$k_\varphi = \frac{Gwt^3}{3l} \tag{17}$$

$$k_L = \frac{k_\varphi}{h^2} = \frac{Gwt^3}{3lh^2} \, , \tag{18}$$

with cantilever length $l$, cantilever thickness $t$, cantilever width $w$, tip height $h$, Young's modulus $E$, Poisson's ratio $\nu$, and shear modulus $G = E/2(1 + \nu)$.

For Si cantilevers the material properties (Young's modulus and Poisson's ratio) are known in any crystal orientation [77].[4] By contrast, the material properties of the $Si_3N_4$ cantilevers are not well defined and may vary significantly due to differences of the chemical vapor deposition processes [78–80]. For instance, Young's moduli and Poisson's ratios of $Si_3N_4$ cantilevers in the range of 120–200 GPa and 0.22–0.27, respectively, have been reported.

Procedures for the reliable calibration of normal forces (i.e. $k_N$) are well established. Several methods can be used, such as the thermal fluctuation method [81–83], the reference lever [84] or the added mass technique [85]. The calibration of the lateral force constant of a given cantilever and the photodiode sensitivity for measurements of lateral forces remained until recently challenging.

The conventional calibration techniques proposed for the calibration of LFM can be grouped into (1) reference methods [86] and (2) two-step [68, 78, 87] procedures. The challenges mentioned arise from the fact that the reference methods suffer from systematic errors introduced by contaminations on the reference samples and that a separate calibration of the lateral force constant $k_L$ and the photodiode sensitivity for lateral deflection $S_L$ is hampered by a number of problems, respectively. The accuracy of the determined value of $k_L$ is limited due to large errors in the determination of the cantilever dimensions and the uncertainty in the values for Young's moduli and Poisson's ratios for $Si_3N_4$ (if applicable). The unavailability of a reliable in situ method to calibrate the photodiode sensitivity $S_L$ and its dependence on factors, including laser beam position on the lever, spot size and asymmetry etc., represent additional complications.

A third group of calibration procedures, (3) the direct (single step) techniques avoids (many of) these problems [88–90]. In particular, the so-called

---

[4] The values of Young's modulus in the [100], [110] and [111] directions are $E[100] = 130$ GPa, $E[110] = 168$ GPa, and $E[111] = 187$ GPa, respectively [77].
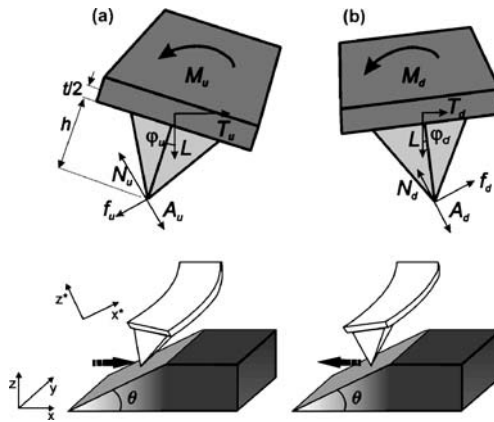
**Fig. 8** Schematic illustration of cantilever torsion while **a** sliding up and **b** sliding down on a sloped surface (in the $x$ direction). While sliding across a sloped surface with angle $\theta$, the acting forces (the applied load $L$, the horizontal tractive force $T$, the adhesion force $A$, the reaction force from the surface acting on the tip with a component $N$ in the surface normal direction and a component $f$ (friction force) parallel to the surface) and the torsion momentum $M$ are in equilibrium and depend on the direction of motion—uphill and downhill, denoted here with subscripts u and d, respectively. $\varphi$ represents the torsion angle of the cantilever, which is proportional to the friction force. $h$ and $t$ stand for tip height and cantilever thickness, respectively. (Reprinted with permission from [91]. © (2006) American Chemical Society)

improved wedge-calibration method, in which a tip/cantilever is scanned across a calibration sample with two well-defined slopes (see Fig. 8), allows one to calculate the calibration factors with an error of ca. 5% [91].

It can be shown that

$$\sin\theta(L\cos\theta + A)\cdot\mu_s^2 - \frac{\Delta_s - \Delta_f}{W_s}(L + A\cos\theta)\cdot\mu_s + L\sin\theta\cos\theta = 0 \quad (19)$$

$$\mu_f = \frac{\alpha W_f}{(L + A)}, \quad (20)$$

where $\mu$ denotes the friction coefficient, $W$ denotes the half width of the friction loop $W = (M_u - M_d)/2$, $\Delta$ denotes the friction loop offsets ($\Delta = (M_u + M_d)/2$) and the subscripts s and f denote sloped and flat surfaces, respectively (see also Fig. 9 below). By solving Eq. 9 for $\mu_s$ two possible mathematical solutions are provided (for any given load and adhesion), corresponding to two values of the friction calibration factor $\alpha$. Since $\alpha$ must be identical for sloped and flat surfaces, we obtain $\mu_f$ from Eq. 20. The physical solution stands for $\mu_s$ and $\mu_f < 1/tg\theta$.

In Fig. 9, topographic and lateral force data obtained on a universally applicable standard specimen is shown that enables one to accurately calibrate
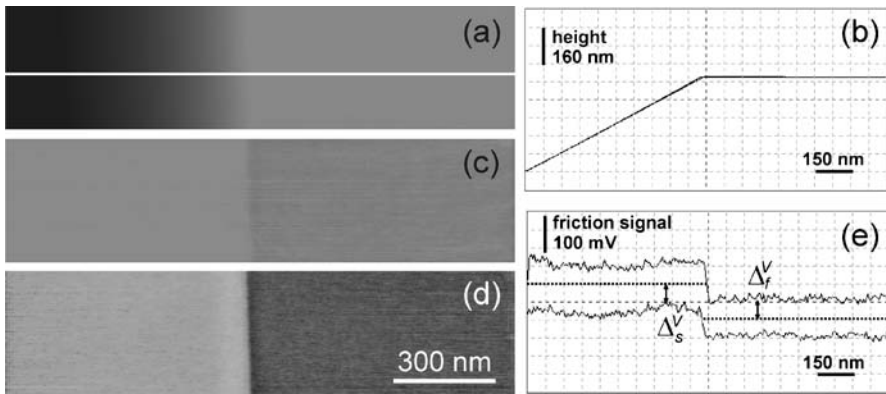
**Fig. 9** Example of experimental data measured with a $Si_3N_4$ tip on both sloped and flat surfaces: **a** topography image (vertical scale from *black* to *white* 800 nm), **b** cross-section of topography (vertical scale 800 nm), **c** difference friction image (trace – retrace, vertical scale 0.5 V), **d** off-set of the friction loops (trace + retrace, vertical scale 0.5 V) and **e** friction loop corresponding to cross-section shown in *panel b* (the off-sets for sloped and flat surface, $\Delta_s$ and $\Delta_f$, respectively, have been marked). (Reprinted with permission from [91]. © (2006) American Chemical Society)

all types of AFM cantilevers and tips for quantitative friction force measurements.

Using this standard and the improved wedge calibration method, calibration factors can be calculated with an error of ca. 5%. The approach is not affected by an additional small sample tilt, different feedback settings, and a possible tip position off the central cantilever axis, as is frequently observed. Only laser light interference and non-spherical tip apex shapes must be taken into account. To illustrate the accuracy of the calibration procedure, nano-tribological results obtained on well-defined micropatterned monolayer surfaces are shown in Fig. 10. Despite the fact that the tips/cantilevers used had a different geometry (V-shaped and single beam) and were microfabricated using different materials ($Si_3N_4$ and Si, respectively), the friction coefficients determined under identical conditions are to within the experimental error the same.

Another important aspect of LFM for its application studies of polymer relaxations and surface dynamics is the controlled variation of temperature and scan velocity, which is related to the frequency of the experiment (see Sect. 1.1) [30]. Temperature and the environment can be controlled and/or modulated using environmental chambers purged with thermostatted gasses of controlled composition and relative humidity (%RH). In addition, heatable sample stages have been applied to control the sample temperature (heatable probe tips are treated in Sect. 2.4). Typical piezoelectric materials used in the AFM scanner withstand temperatures of <60 °C and %RH < 65% (see specifications of the particular material used), which limits the range of at-
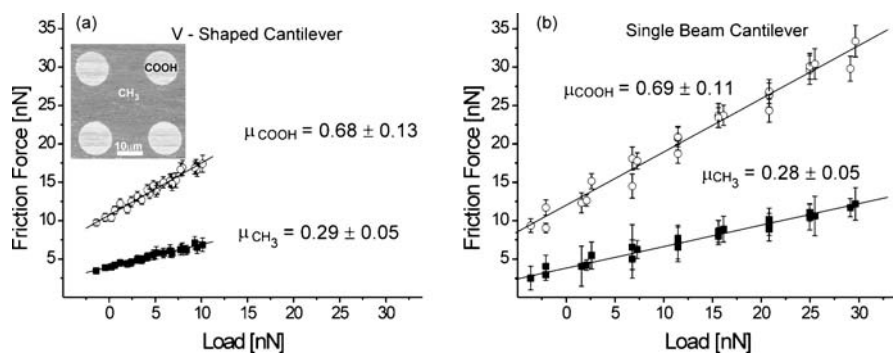
**Fig. 10** Friction force versus load for a micropatterned SAM sample (exposing – CH$_3$ and – COOH head groups, respectively, see *inset* in **a**) measured using two different Si$_3$N$_4$ cantilevers: **a** V-shaped and **b** single beam, with scanning velocity of 40 μm s$^{-1}$ at 50% RH and 25 °C. The *solid lines* correspond to linear least squares fits. The *error bars* indicate the standard deviation ($n = 128$) of the data analyzed for a given load (Adapted and reprinted with permission from [91]. © (2006) American Chemical Society)

tainable conditions. The frequency can typically *not* be varied over a broad range while keeping nanoscale resolution using the piezo transducer of the AFM, due to increased noise level, inaccurately operating feedback loop and decreasing pixel resolution as a result of large scan sizes. As an alternative, additional sample actuation stages based on stacked shear piezos [92] or other actuators, such as quartz crystal microbalances [93], have been reported, which allow one to achieve scan velocities of >1.0 μm s$^{-1}$ and ~10$^{-1}$ m s$^{-1}$, respectively (for an example, see Fig. 11).
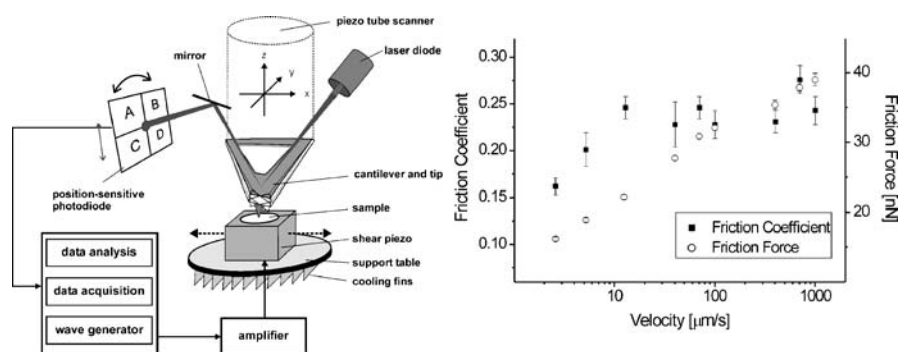


**Fig. 11 a** Schematic of a high velocity AFM set-up comprising a commercial stand-alone atomic force microscope, the high velocity accessory and peripheral devices for accessory operation, data acquisition and signal processing (not to scale). **b** Friction coefficient for oxidized Si(100) and Si$_3$N$_4$ tip as a function of velocity measured in a nitrogen atmosphere (<3% RH) at room temperature (25 °C). (Reprinted with permission from [92]. © (2005) American Institute of Physics)

According to Sect. 1, the investigation of friction and surface dynamics of polymers requires careful control of the temperature and the frequency (rate) of the experiment. In addition, the acquired data must be quantitative and hence robust calibration methods must be applied (see above). On top of these requirements a number of important aspects must be considered in the analysis of friction force microscopy data. Comparisons among data from different labs is only viable, if all these points have been taken into account.

One crucial issue is the difference between the *load* applied with the LFM cantilever and the total force in the surface normal direction in the nanoscale contact, the so-called *normal force*. The normal force is defined as the sum of load and adhesion force (e.g. assessed in a $f$–$d$ experiment, see Sect. 2.3.1). Since friction force and contact area are directly related for single asperity contacts, it is important to take this effect into account, as well as the effect of different contact pressure. The forces due to capillary condensation between tip and sample can be avoided by operation of the AFM in vacuum or under conditions of dry inert gas.

The pressure is given by the normal force divided by the (experimentally not determined, i.e. unknown) true tip–sample contact area. The latter quantity is critically related to the radius of curvature of the probe tip. The value of this radius, which must be carefully calibrated, also determines the time during which tip and sample interact. Such a calibration can be performed by analyzing electron microscopy images or AFM images taken on a reference grating exposing very sharp spikes of known radius of curvature (Fig. 12).

Finally, although noted by various authors to be difficult, care must be taken to ensure an operation in the elastic regime. Local plastic deformation of the polymer sample specimen must be avoided, because in this case ploughing terms (Eq. 4) must be considered as well.
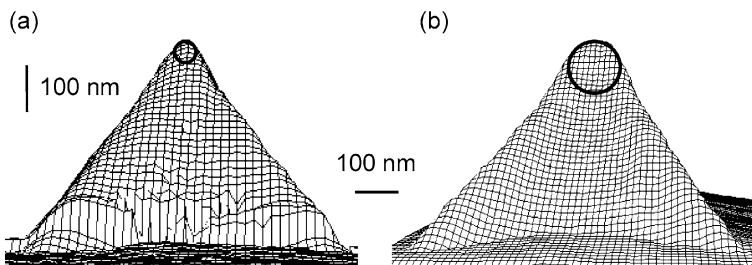


**Fig. 12** Images (obtained by contact mode AFM on a calibration grating) of **a** a sharp and **b** a flat tip apex. The tip radii $r$ determined for **a** and **b** were 25 nm and 60 nm, respectively. (Reprinted with permission from [91]. © (2006) American Chemical Society)

## 2.2
## Other Scanned Probe Methods to Assess Polymer Relaxation Phenomena

### 2.2.1
### Shear Modulation Force Microscopy (SM-FM)

In shear modulation force microscopy (SM-FM) a sharp probe tip, which is kept in contact with the sample (typically applied load is on the order of nN to tens of nN), is laterally modulated with a nanometer scale amplitude $\Delta x_i$ (Fig. 13). This amplitude is chosen such that any tip–sample slipping is avoided. Therefore SM-FM is considered a non-scanning technique. Non-scanning conditions are important to avoid significant scanning-induced changes in the tip–sample contact area. Using lock-in techniques, the modulation response, $\Delta x_R$, is analyzed relative to $\Delta x_i$. For a small (in-plane) lateral displacement for a sphere-plane geometry (assuming the absence of slip), the lateral stiffness of the contact $k_{c,x}$ is provided as [94–96]:

$$k_{c,x} = 8aG^* \tag{21}$$

with

$$G^* = \left( \frac{2 - \nu_1^2}{G_1} + \frac{2 - \nu_2^2}{G_2} \right)^{-1}, \tag{22}$$

with the radius of the contact area $a$, the shear moduli of the sample and the probing tip $G_1$ and $G_2$, respectively, and the corresponding Poisson's ratios $\nu_1$
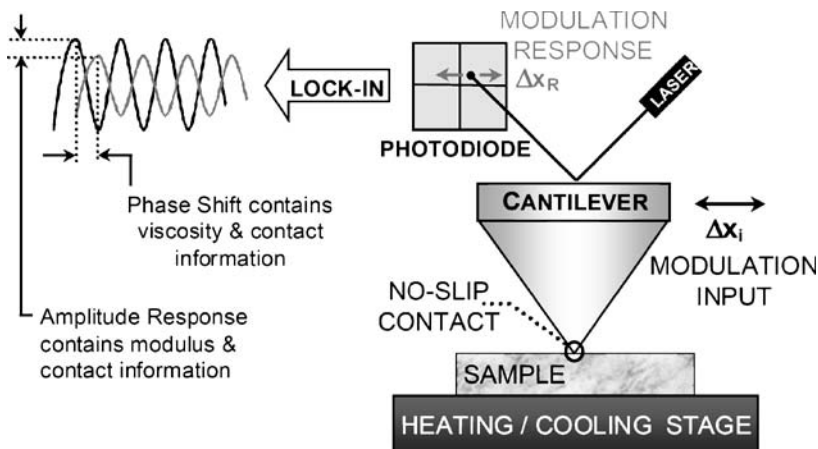


**Fig. 13** Schematic diagram of a shear modulation force microscopy experiment. (Reproduced with kind permission of Springer Science and Business Media from [96]. © (2005) Springer)
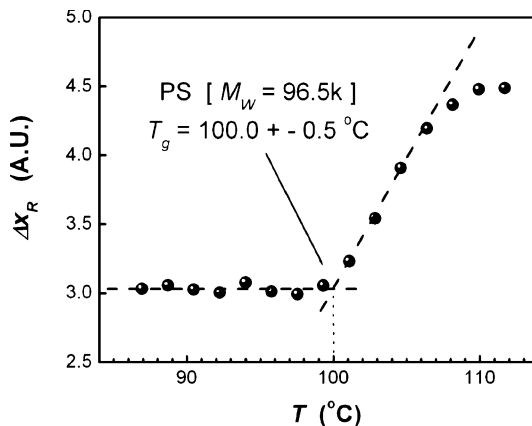
**Fig. 14** Determination of the glass transition temperature of polystyrene by SM-FM: modulation amplitude response vs. temperature plot. (Reproduced with kind permission of Springer Science and Business Media from [96]. © (2005) Springer)

and $\nu_2$ [17]. The total lateral elastic constant $k_{tot,x}$ can be written as:

$$\frac{1}{k_{tot,x}} = \frac{1}{k_{c,x}} + \frac{1}{k_T} , \qquad (23)$$

where $k_{c,x}$ and $k_T$ denote the lateral contact stiffness and the torsional cantilever stiffness, respectively.

As for most AFM approaches, the true contact area (radius $a$ in Eq. 21) is difficult to assess and the precise determination of the cantilever stiffness $k_T$ limits the overall accuracy of the data. Sills and Overney pointed out that these shortcomings are not relevant for simple thermorheological studies (e.g. the determination of $T_g$). In a typical experiment, the stationary AFM tip rests on the polymer (with a pre-set load). The sample temperature is increased in small increments and following equilibration the response $\Delta x_R$ is measured. The tip–sample contact area thus changes only as a consequence of temperature-induced changes, e.g., in the polymer's modulus. A plot of $\Delta x_R$ versus temperature exhibits a "kink" at a temperature assigned to $T_g$ (Fig. 14).

## 2.2.2
## Scanning Viscoelasticity Microscopy (SVM)

A related technique, termed scanning viscoelasticity microscopy (SVM) was introduced by Kajiyama and co-workers (Fig. 15). SVM is a (scanning) contact mode AFM technique; similar to SM-FM (Sect. 2.2.1) the sample is modulated with several kHz, albeit in surface *normal* direction [97]. When the tip exerts a force on the surface (corresponding to a deflection characteristic for
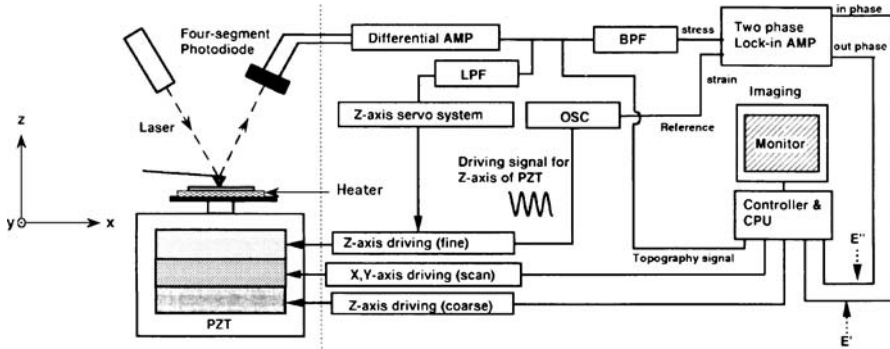
**Fig. 15** Schematic of scanning viscoelasticity microscopy used for imaging of dynamic viscoelasticity by AFM. (Reprinted with permission from [97]. © (1994) American Chemical Society)

the repulsive force region of a $f-d$ curve), the sample surface is deformed by the tip. The vertical modulation of the sample position results in a concomitant modulation of the cantilever deflection, which depends on viscoelastic properties of the sample. The phase difference between the modulation signal of the sample position and the modulated response of the tip corresponds to the mechanical loss tangent, $\tan\delta$, of the probed surface region.

## 2.2.3
## Force Modulation Microscopy (FMM)

Force modulation mode (FMM) AFM is a contact mode technique that allows one to resolve lateral differences in modulus [98, 99]. In FMM AFM, the cantilever is excited by a bimorph to oscillate at a frequency of tens of kHz (which is below its resonance frequency), while it scans the surface in contact mode. By monitoring the oscillation amplitude, the elastic modulus of the surface can be mapped with high resolution. Depending on the corresponding moduli, the contrast in the amplitude image reveals high modulus (i.e. large amplitude) and low modulus (i.e. lower amplitude) areas [100]. Recently, the use of frequency dependent FMM AFM has been described, where selective contrast can be achieved in heterogeneous systems [101, 102]. A practical limitation for the approach in the field of polymers is the fact that shear forces, similar to contact mode, may cause sample damage or distortion of the underlying morphology.

## 2.2.4
## Scanning Local Acceleration Microscopy (SLAM)

In scanning local acceleration microscopy (SLAM) the position of the sample is modulated at frequencies *above* the highest system resonance [103].

This provides, as shown in the literature, the clearest difference in cantilever response for the variations in elastic modulus of stiff samples. Experimentally, to a standard AFM set-up a high-frequency transducer is added, which is positioned underneath the sample. The ultrasonic vibrations, generated by a high frequency function generator connected to the transducer, are transmitted through the sample and are detected via the AFM cantilever. The signal is sent to a lock-in amplifier and the output of the lock-in is utilized to generate an image simultaneously captured with the conventional AFM (height) image. Using a small-amplitude continuous sine wave, to which the cantilever responds sinusoidally, provides access to spatially resolved variations in the interaction stiffness, which is related to the elastic modulus of a stiff sample.

### 2.2.5
### Torsional Resonance (TR) Mode AFM

Torsional resonance (TR) mode AFM is a recently introduced AFM mode that exploits the torsional resonance amplitude (or phase) of a stiff cantilever to control the feedback loop (i.e. to maintain the tip/surface relative position through lateral interaction) [104]. This mode provides complementary information to intermittent contact (tapping) mode for surface imaging and studies. The nature of tip/surface interaction of the TR mode facilitates phase measurements to resolve in particular the in-plane anisotropy of materials, as well as measurements of dynamic friction at nanometer scale. Recently, various models have been proposed to extract useful physicochemical parameters, thus paving the route to quantitative measurements of contact stiffness, elastic moduli and friction, from the data [105, 106].

### 2.3
### Normal Force Techniques

### 2.3.1
### Force–Distance Curves and Determination of Pull-Off Forces

The interactions between the tip and the sample surface can be measured using the force spectroscopy mode of AFM [107, 108]. In the experiment the sample is moved up and down (in and out of contact with the tip). A schematic force–displacement curve ("force curve") thus obtained is shown in Fig. 16.

During the approach (loading) part (position 1–2), no interactions occur between the tip and the sample surface. As the tip-surface distance becomes sufficiently small, the gradient of the attractive force overcomes the cantilever spring constant and brings the tip in contact with the sample surface (position 3). Further approaching causes a deflection of the cantilever (position 3–4). The unloading part of the force–displacement curve starts from pos-
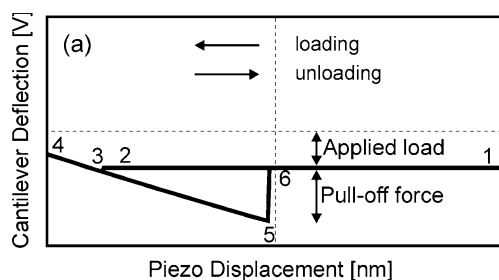
**Fig. 16** Schematic AFM force-displacement curve

ition 4, the deflection of the cantilever is decreased as the sample surface retracts from the tip. When the sample surface is further withdrawn from the tip, the cantilever is deflected owing to adhesive forces. At position 5, the elastic force in the cantilever overcomes the force gradient and the tip snaps off
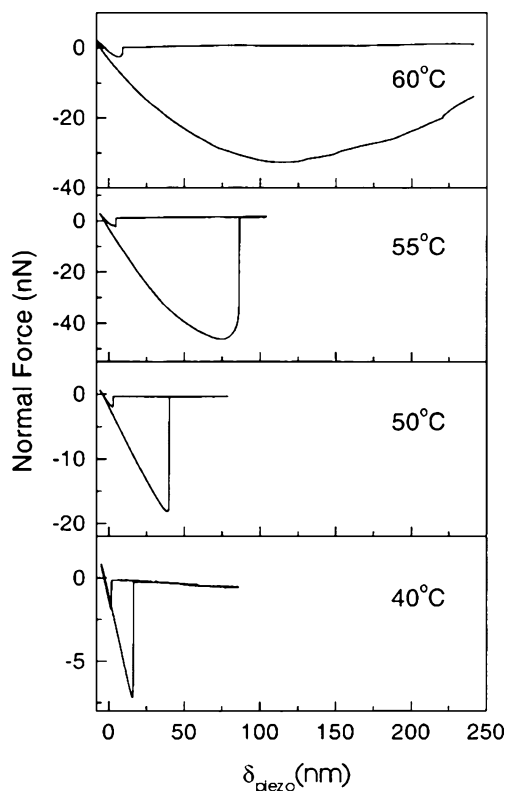


**Fig. 17** $f-d$ curves obtained at different temperatures on a poly($tert$-butyl acrylate) film at constant probe rate $f = 125$ Hz. (Reprinted with permission from [109]. © (2000) American Chemical Society)

from the surface (position 6). From position 6 to 1, the cantilever returns to its equilibrium position. The adhesion between tip and sample is characterized by the so-called pull-off or pull-out force (snap off). The pull-off force is related in current continuum contact mechanics models to the work of adhesion, which may, in the case of polymers, be temperature and rate-dependent (compare Eqs. 9 to 12). In addition, neck formation between the polymer and the retracting probe may alter the $f$–$d$ curves in a characteristic manner (see Fig. 17) [109].

## 2.3.2
## Indentation Measurements

In the $f$–$d$ measurements discussed in the previous section one can also analyze the part of the curves corresponding to tip–sample contact. Using these so-called AFM indentation measurements the Young's modulus of the underlying polymer sample can be determined as a function of temperature and loading rate (~frequency). As alluded to above, one records $f$–$d$ curves employing a cantilever with appropriate spring constant (stiffness lever ~ stiffness sample). The $f$–$d$ curves can be analyzed according to various indentation models, e.g. the Hertz model (Sect. 1.2), to calculate the Young's
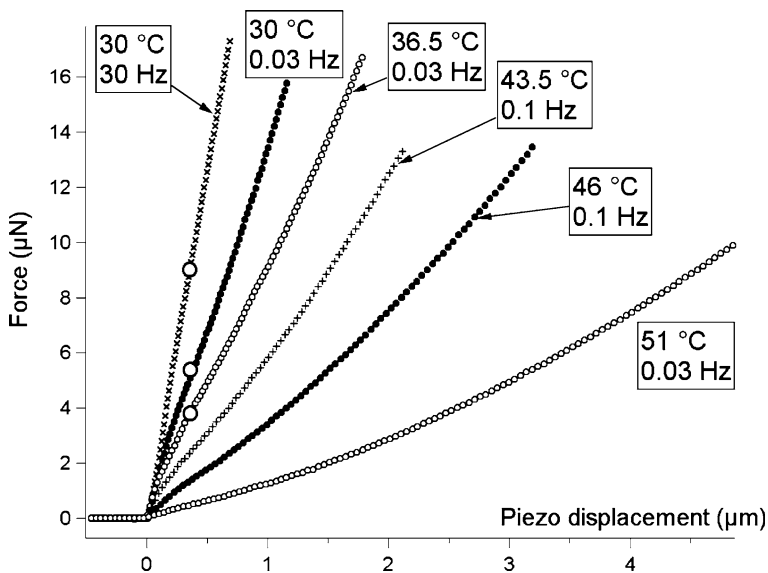


**Fig. 18** Approach parts of the $f$–$d$ curves recorded on poly($n$-butyl methacrylate) samples at various rates and temperatures. The different slopes of the indentation curves represent different moduli of the polymer ($T_g = 22\,°C$). (Reprinted with permission from [110]. © (2005) American Chemical Society)

modulus. At the glass transition temperature, the modulus will change by several orders of magnitude, as mentioned. Hence the $T_g$ in polymer films and its possible dependence on various factors, including film thickness, relative humidity (with water as a plasticizer) etc. can be quantitatively captured [110].

## 2.4
## Scanning Thermal Microscopy

In scanning thermal microscopy a heatable probe tip is used. Early examples include relatively blunt probes (the area of this heat source is approx. 1 µm × 0.25 µm) comprising a Wollaston wire (Fig. 19a). More recently, microfabricated heatable cantilever/probe tip assemblies have become commercially available that push the resolution to the sub-100 nm scale due to their sharp integrated tips (Fig. 19b) [111, 112]. Using such probes, the indentation of the probe into the polymer can be recorded as a function of temperature. Hence, transitions, such as the glass transition, can be inferred from the softening of the polymer. However, as has been noted, tip penetration and polymer expansion may, depending on the load and the contact area, lead to an upwards bending of the lever [113].
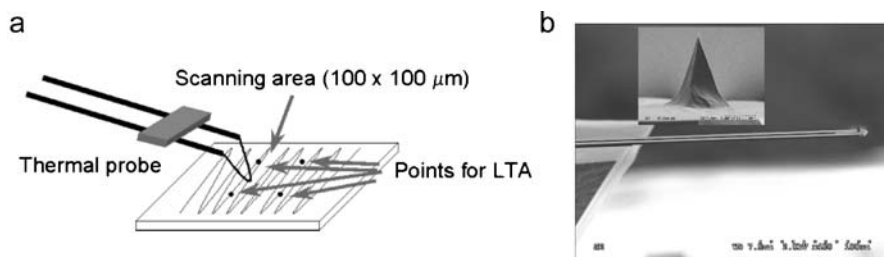
**Fig. 19** **a** Schematic of a local thermal analysis experiment using a Wollaston wire probe equipped with a mirror. Within the scanned area the probe may record phase changes in the polymer film via heated tip-induced changes in modulus. (Reprinted with permission from [113]. © (2005) American Chemical Society). **b** SEM image of the microfabricated thermal probes for high resolution thermal analysis (*inset*: SEM image of the actual probe tip). (Reproduced with kind permission from Anasys Instruments Inc.)

## 3
## Friction and Surface Dynamics of Polymers on the Nanoscale

Dynamic friction on polymers has a large contribution from internal viscoelastic dissipation, which is ultimately related to polymer relaxation processes. Using the experimental approached briefly introduced in Sect. 2, var-

ious aspects of friction and surface dynamics ranging from fundamental studies of chain dynamics and glass temperatures in ultrathin polymer films to the mapping of multiphase systems can be addressed.

In particular, one can differentiate friction and chain dynamics at the surface of polymers vs. the bulk, relaxations in (ultra)thin film systems (confinement effects), interface effects such as pinning and possible effects of sample history. Despite a large body of literature the current view on these issues is still controversial, thus known approaches must be refined and new approaches must be developed to provide additional insight to contribute to solve the open questions (for suggested behavior see Fig. 20).

In this context it is important to reiterate that relevant data can only be obtained if the measured quantities are assessed quantitatively (i.e. proper calibration is required) and that all important external factors are controlled and have been taken into consideration. This refers to the elastic vs. plastic contact regime, the load vs. normal force issue, the contact pressure (incl. tip radius) as well as control of both temperature and true frequency (scan rate and tip–sample contact length) etc. In particular, it is also necessary to consider the penetration or information depth of a particular method. To be able to assess, e.g., the proposed $1-2$ nm thin surface layer of reduced density (Fig. 20), care must be taken to probe this very layer and not the film interior. In parts, these requirements mandate new technical developments, such as the mentioned velocity control using external high rate actuators, that became only recently available.
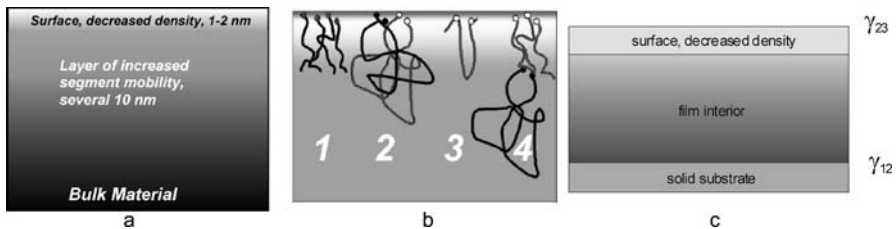


**Fig. 20 a** Schematic of the surface of a glassy polymer that possesses a thin layer of reduced density at the surface followed by a layer of increased mobility of polymer segments changing smoothly to the bulk material. **b** Schematic depicting possible mechanisms of lowering the $T_g$ close to surfaces: (*1*) excess free volume induced by surface enrichment of end groups, which causes an enhanced mobility of chain segments and a lower polymer segment density, (*2*) confinement of polymer chains for polymers with high $M_n$ which causes a break in symmetry at polymer surfaces (flattened chain conformation) and chain confinements in films with $d < R_g$, (*3*) increased collective motions along the chain (loop motions), which require a weaker free volume and does not involve chain ends, (*4*) enrichment of low molecular weight fraction at the surface. (Reprinted with permission from [113]. © (2005) American Chemical Society). **c** Interfacial interactions in (ultra)thin films characterized by the substrate–polymer interfacial free energy and the polymer–air interfacial free energy

## 3.1
## Mapping of Multiphase Systems

An obvious application area of AFM that relies on friction and surface dynamics is the study of heterogeneous systems. While there are many AFM modes that combine high spatial resolution with a contrast mechanism that is sensitive to a particular polymeric phase in a multiphase system (e.g. intermittent contact mode phase imaging, which is sensitive to differences in energy dissipation) [114], LFM, SVM, $f$–$d$ curve acquisition as well as other AFM modes provide in some cases better access to maps of the local viscoelastic properties. These maps in turn yield access to estimates of surface coverages, morphologies and localization of particular components in complex multiphase systems.

In the so-called chemical force microscopy (CFM) approach [115, 116], in which AFM tips exposing defined surface chemistry are utilized to assess differences in surface chemical composition using e.g. local friction differences (related to interactions between functional groups or atoms exposed on both tip and sample surface as contrast), different polymers have been successfully differentiated. Examples include the differentiation of polyamide-rich regions from poly(ethylene glycol)-rich regions in a blocky segmented copolymer using self-assembled monolayer-coated tips reported by Sinniah et al. [117] and differentiation of a phase-separated blend of polystyrene (PS) and poly(methyl methacrylate) imaged with gold-coated and silicon oxide coated tips in perfluorodecalin [118]. In this latter work Feldman et al. exploited the selective amplification of the dispersive van der Waals interactions in perfluorodecalin to obtain predictable interactions and thus contrast.

Werts et al. reported on successful CFM imaging of the microphase-separated domain structure in PS-poly(vinyl pyridine) hetero-arm star copolymer, thus implying a lateral resolution of better than ~30 nm [119]. The friction contrast measured in an argon atmosphere was well-pronounced with a carboxylic acid-functionalized tip, as shown in Fig. 21.

Using conventional LFM, phase-separated blends of PMA and PMMA, i.e. components possessing $T_g$'s that are close to (287 K) and far above (390 K) the temperature at which the experiment was carried out (295 K), were studied by Lee [120]. While PMMA did not show a dependence of lateral force on scan rate (at a constant load of 5 nN), PMA showed a monotonically decreasing behavior. These observations are consistent with the interpretation that in the glassy state the elastically deformed surface is immediately recovered and the dissipated energy is small. By contrast, for the PMA, at a temperature close to its bulk $T_g$, a substantial fraction of the energy involved in the deformation at the contact is dissipated. Thus, in phase-separated blends, the two phases were distinguished in scan rate-dependent measurements.

Cappella and Kaliappan measured force–displacement ($f$–$d$) curves on PS/PnBMA blends (sandwich of PS and PnBMA) as a function of tempera-
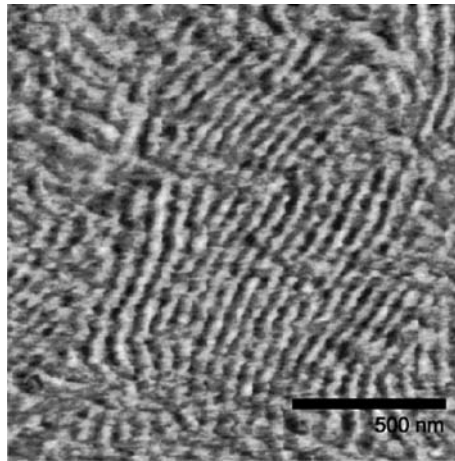
**Fig. 21** Friction force image (1.5 μm×1.5 μm) obtained by means of CFM with a COOH tip. Using this tip functionality the friction coefficient is higher for the PVP part of the copolymer, which reveals the morphology as the alternating *bright* (high friction, PVP) and *dark* (low friction, PS) areas. (Reprinted with permission from [119]. © (1998) Wiley-VCH)

ture. In their experiments these authors focused on the determination of local mechanical properties (Young's modulus) of these polymers with a spatial resolution of 800 nm, i.e. on the influence of morphology on the mechanical properties of the model blend/sandwich structure in the vicinity of the interface. Exploiting a new analysis technique based on Hertz theory (Sect. 1.2), the corresponding moduli were obtained. A transition region was revealed (Fig. 22), where the Young's modulus decreases gradually from the value of PS to the value of PnBMA [121].

On bilayer films composed of PS (top layer) and PI (lower layer) Satomi and coworkers studied how far buried layers influence the surface viscoelasticity as assessed by scanning viscoelasticity microscopy (SVM). The surface dynamic storage modulus, $E'$, decreased with decreasing thickness of the upper PS layer due to the contribution from the soft underneath PI layer once the upper layer thickness fell short of 70 nm. On the contrary, surface $E'$ was invariant for the bilayer with a thicker upper layer. These results indicate that the stimulus displacement imposed propagates to a depth of at least 70 nm along the surface normal at room temperature [122].

The elastic and viscoelastic properties blends of PP and ethylene-propylene (EP) were investigated with the force modulation technique by Nysten et al. In addition to a mapping of the distribution of the rubbery nodules of EP at the surface, the sub-surface distribution of these nodules could be estimated [123, 124]. While the FMM data yielded qualitative data, more recent indentation mapping based on force-displacement curves al-
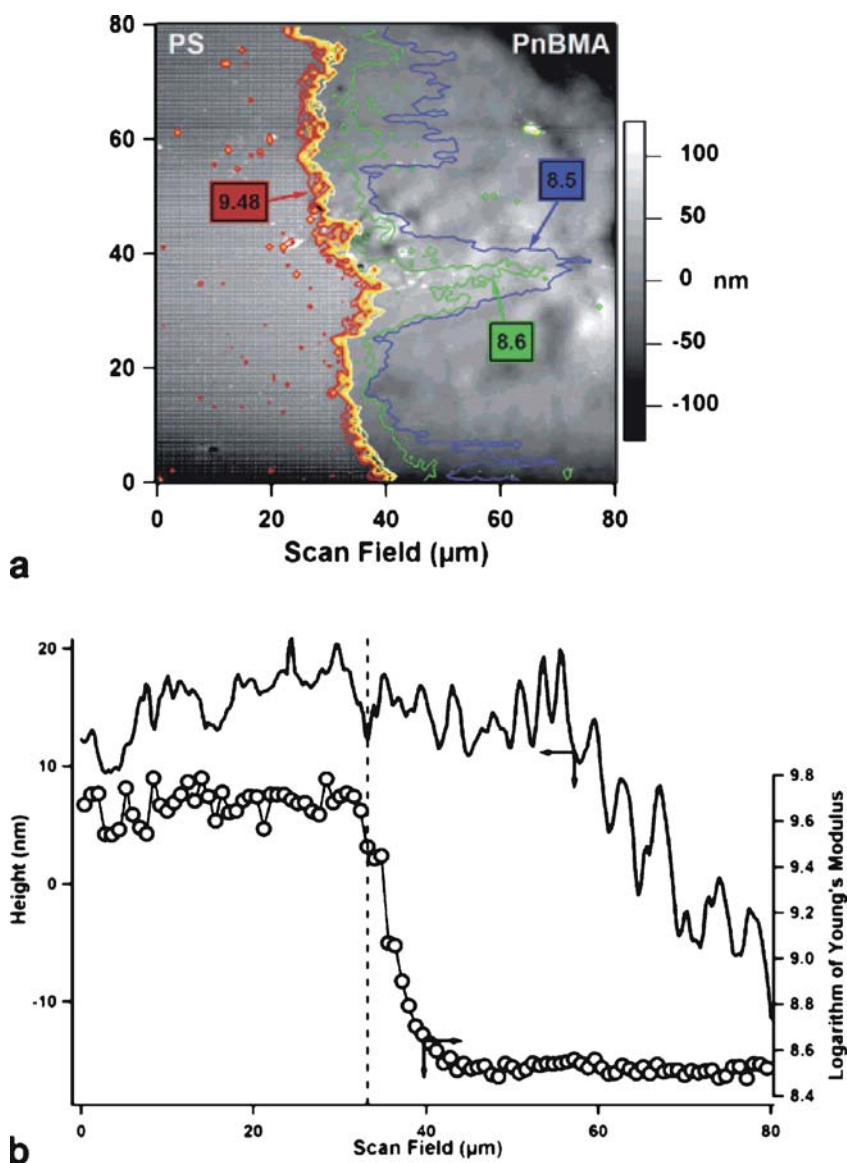
**a**



**b**

**Fig. 22 a** Topographic image (*gray scale*) of the model blend at the interface at 57.4 °C and superimposed profiles of log($E$) = 9.48 (*dark red line*), down to log($E$) = 9 (*light yellow line*), in steps of 0.08 (*lines of increasing brightness*, very close to each other and bunched together at the interface). Also the profiles of log($E$) = 8.6 (*green line*) and of log($E$) = 8.5 (*blue line*) are shown. **b** Line profile of the topography (referred to *left axis*) and of log($E$) (referred to the *right axis*) of the model blend across the interface. It can be seen that there is no discontinuity in the topography at the interface and also that the topography does not influence the determined Young's modulus. (Reprinted with permission from [121]. © (2006) American Chemical Society)

lowed Nysten et al. to obtain quantitative information of the surface elastic modulus [125].

The application of different AFM modes to measure the nanoscale elastic and viscoelastic properties of PMMS/rubber nanocomposites was reported by Cuberes et al. [126] In particular, heterodyne force microscopy (HFM) with ultrasonic force microscopy, FFM and force modulation microscopy were compared. The authors concluded that the combination of different AFM-related techniques helped to interpret the images with respect to the rather complex local structure of the polymer blend in rubber toughened PMMA. Amplitude-HFM resolved differences in local sample stiffness due to the presence of rubber in the near-surface region, while phase-HFM distinguished small differences in viscoelastic and/or adhesion hysteresis response time of PMMA on top of the rubber.

Oulevey et al. discussed dynamic mechanical analysis at sub-micrometer scales based on experiments with local DMA and variable temperature scanning local acceleration microscopy (SLAM) [127]. Primary and secondary relaxations in various polymer materials (PES/SAN and PS/PMMA blends, also PMMA, PS and PTFE) were observed as a function of temperature. The lateral resolution of SLAM was reported to be better than 100 nm.

## 3.2
### Polymer Relaxations, Chain Dynamics and Viscoelasticity

One important fundamental question to be answered is related to the difference of chain dynamics among the bulk and the surface. Using various LFM and related approaches polymers can indeed be probed at the surface and down to various depths; thus this and other related issues can be directly addressed. Depending on the operation conditions and thus indentation depth, AFM probes a given polymer sample always at the surface and may sample into the near-surface region of reduced density (Fig. 20). These measurements have immediate practical relevance as in polymer films, for instance, the structural, material, and transport properties become increasingly dominated by interfacial, conformational, and dimensional constrains, when the thickness is reduced to the sub-100 nm scale (see Sect. 3.3) [1–3]. In addition, rheological gradients near the interfaces can lead to a behavior that deviates from the bulk. Relaxation properties can be influenced and enhanced conformational stability may be achieved through control of the interfacial conditions, molecular weight, crosslinking density, and film thickness [3, 28].

On the basis of fluorescence microscopy data obtained on sandwich samples [128, 129] or in single-molecule fluorescence measurements [130] an improved understanding of the dynamics in thin and ultrathin polymer films, and in particular the role of the interfaces (compare Fig. 20) has emerged. The depression or increase in glass transition temperature, as a confinement ef-

fect of thin substrate-supported polymer films (discussed in more detail in Sect. 3.3), has been attributed by various authors to effects that stem from the substrate–polymer and polymer–vacuum interface, respectively. These studies revealed that the enhancement of dynamics at the free film surface may affect $T_g$ several tens of nanometers into the film [128]. These observations of enhanced mobility of macromolecules at the film surface also point to lowered activation energies and increased frequencies of the relaxation processes involved (compare Figs. 1 and 2).

Studies of polymer relaxations, chain dynamics and viscoelasticity at the surface by AFM-based approaches rely on different types of experiments, in which, depending on the authors, different parameters were determined and different effects that interfere with the interpretation of the data were taken into account. In the following we will review the central results obtained in investigations that targeted mainly the $\alpha$-transition ($T_g$), but also various sub-$T_g$ transitions ($\beta, \gamma$). To exclude effects of the underlying solid substrate, films with thicknesses of 100 nm or larger are considered.

Pu et al. studied PS films on silicon with shear modulation force microscopy (SMFM) and concluded that the surface $T_g$, determined in amplitude vs. temperature plots (Fig. 23), is not different from the bulk under the conditions investigated [131]. In addition, these authors show that the values of the $T_g$'s obtained for samples of various thicknesses do not depend to a noticeable extent on the load applied, which was varied by a factor of 3, the modulation frequency and drive amplitude over a substantial range.

These data are supported by work of Sills et al. who determined surface $T_g$ values in LFM measurements by analyzing friction force-velocity isotherms
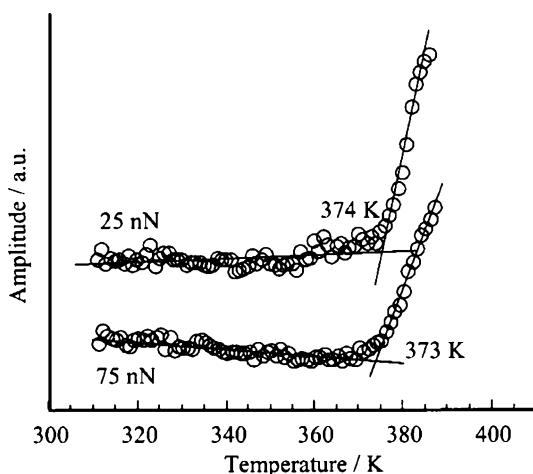


**Fig. 23** $\Delta X$ vs. temperature curves for PS ($M_w = 1230\,$k) in a thick film on silicon at applied loads of 25 and 75 nN. The $T_g$ was determined from the analysis of the kinks shown (reproduced from [131]. © (2001) American Chemical Society)

and application of the time–temperature superposition principle. From the master plot and an Arrhenius plot of the shift factors an activation barrier of 81 kcal mol$^{-1}$ was determined that coincides with the (bulk) value 80–90 kcal mol$^{-1}$ for the $\alpha$-transition in PS (96.5 kg mol$^{-1}$) [132]. In a different study the $\gamma$-relaxation (rotation of phenyl groups) was interrogated by Sills and Overney in atactic PS by LFM at different temperatures and scanning velocities (Fig. 24). The activation energy thus determined ($E_a = 7$ kcal mol$^{-1}$) was similar to reported bulk data [133].

A similar conclusion was reached by Kaliappan and Cappella, who also studied PS, albeit in force–displacement measurements. From data acquired at different temperatures and tip approach/retraction rates the Young's moduli and the yielding forces were determined. The calculated WLF coefficients for temperatures above $T_g$ and the activation energy below $T_g$ exhibited good agreement with published (bulk) literature values [134].

Similarly, Bliznyuk et al. determined the glass transition of PS ($M_n$ from 3900 to 1 340 000, polydispersity 1.05–1.15) via the acquisition of $f$–$d$ curves at various temperatures [135]. The values of the surface glass transition reported by these authors for the samples with $M_n > 30 000$ were also consistent as the corresponding bulk values. However, low molecular mass polymers were concluded to behave differently. Chain entanglement variations were held responsible for the observed surface $T_g$ depression effect rather than the end group localization at the free surface.

Hence several independent measurements concluded that the glass transition temperature in PS (except for possibly low molar mass) is *not* altered in the probed surface-near region. The probed depth is in all these studies a function of the tip radius and, more importantly, the applied load. The load, as shown in Fig. 23, was for the SFMM experiments substantial. Similarly, in the studies of Sills and co-workers, as well as Kaliappan and Cappella a sig-
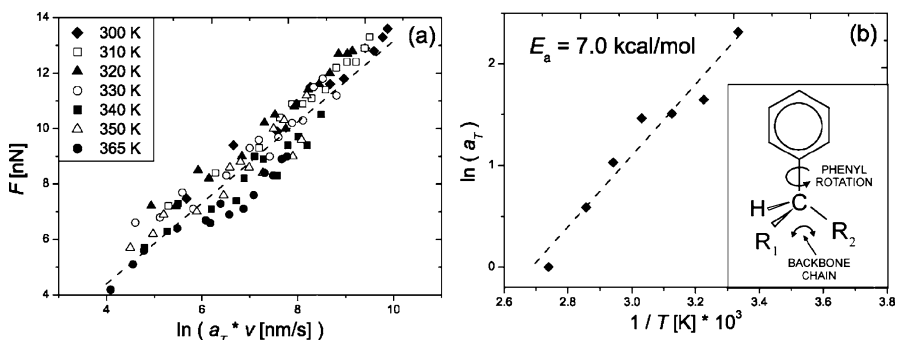


**Fig. 24 a** Superposed friction master curve; **b** thermal shift factor $a_T$. An activation energy $E_a$ of 7.0 kcal mol$^{-1}$ is deduced from the slope of the regression line, corresponding to the activation of phenyl rotation in atactic PS (*inset*). (Reprinted Figure with permission from [133]. © (2003) by the American Physical Society)

nificant contribution of the adhesive force to the normal force of 91 nN and loads of several $\mu$N, respectively, were reported.

Similar to these data on PS, several groups reported unaltered surface $T_g$ values for PtBuA and PnBMA, relying on adhesion measurements at different temperatures and probe rates, and the subsequent application of the time–temperature superposition principle on the one hand [109], and the determination of the Young modulus and yielding force in the vicinity of $T_g$, as a function of temperature and/or probe rate, on the other hand [110]. These reports thus also support the notion that the molecular relaxation of the polymer sample at the free surface, under the conditions probed, is not noticeably different than that of the bulk.

In contrast to these reports, the group of Kajiyama has reported in numerous publications on the enhanced macromolecular mobility observed at the surface of polystyrene films and the dependence of the observed decreased surface $T_g$ on factors, including molar mass, chain-end chemistry and structure, entanglements and polydispersity [136–139]. For example, in 200 nm thick films of monodisperse PS ($M_n$ from 4900–1 460 000, and binary PS blends with different $M_n$) on silicon measurements of the lateral force (under an applied load of 10 nN) vs. temperature at a given scan rate indicated that the surface $T_g$ of the PS films was markedly lower than the corresponding bulk $T_g$ over the entire molecular weight range. The surface $T_g$ was determined from the maximum observed in friction force vs. temperature plots (Fig. 25a). In addition, the apparent activation energy of the surface segmental motion in PS was determined as $230 \pm 10\,\mathrm{kJ\,mol^{-1}}$, which is significantly smaller than the reported bulk value that ranges from 360 to $880\,\mathrm{kJ\,mol^{-1}}$ (Fig. 25b,c). Finally, these authors showed a surface enrichment of the shorter chain component in the blend films that becomes more pronounced with an increasing molar mass dispersity between the two components due to entropic effects [140]. Consistent observations of depressed surface $T_g$ values as assessed by the same group using SVM were also reported [139], as well as direct SVM observation of a softening in monodisperse PS films on Si that were partly scratched by a blade [141].

The results of Kajiyama et al. are in line with the data of Hammerschmidt et al. who concluded, based on velocity and temperature-dependent LFM measurements, a lowered surface $T_g$ for PS [30]. These authors also measured the friction force between a Si tip and a PMMA surface for four different velocities between 2 and $220\,\mu\mathrm{m\,s^{-1}}$. A peak in friction force was observed for measurements at 25 °C, which shifted towards higher velocities at increasing temperatures. This peak was attributed to the $\beta$-relaxation process (compare Fig. 1). These authors also observed a lower activation energy for this process as compared to reported bulk values ($50\,\mathrm{kJ\,mol^{-1}}$ vs. $71$–$96\,\mathrm{kJ\,mol^{-1}}$). However, this process attributed to the $\beta$-relaxation occurred at a similar temperature and a similar frequency as in the bulk, which is apparently inconsistent with the concluded higher mobility at the surface (compare Fig. 2).
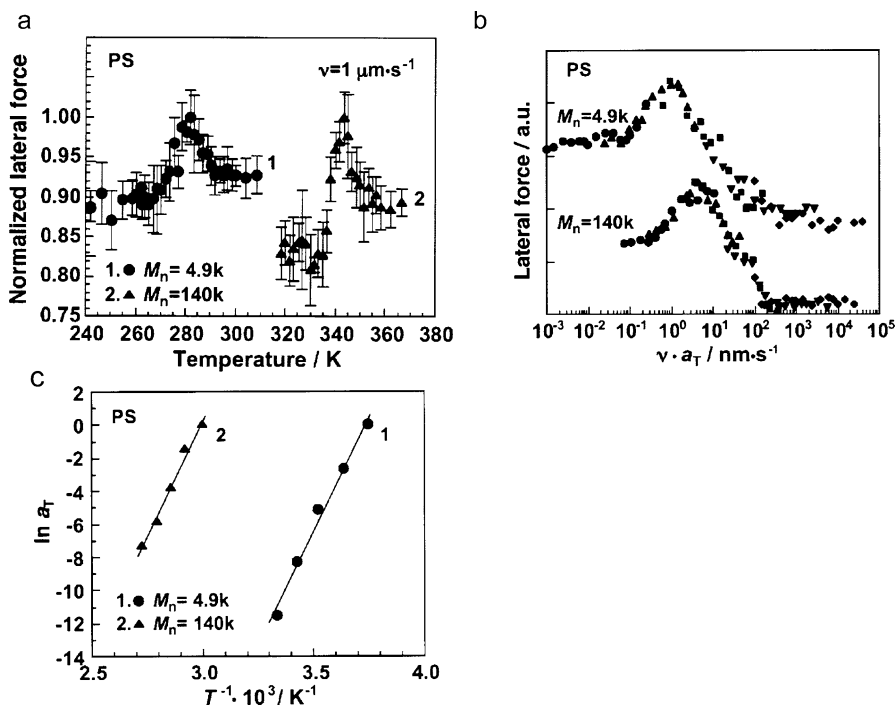
**Fig. 25 a** Typical lateral force/temperature curves at a given scanning rate. Curves for PS with $M_n = 4900$ or $M_n = 140\,000$ at a scanning rate of $1\,\mu m\,s^{-1}$ are displayed. The bulk $T_g$ values measured by DSC are 348 and 376 K, respectively. **b** Master curves of the scanning rate/lateral force relationship for PS films drawn from each curve in Fig. 4. Reference temperatures of 267 and 333 K have been used for PS with $M_n = 4900$ and for PS with $M_n = 140\,000$, respectively. **c** Semi-logarithmic plots of $a_T$ versus the reciprocal absolute temperature ($T^{-1}$) for PS films with $M_n = 4900$ or $M_n = 140\,000$. (Reprinted with permission of John Wiley & Sons Inc. from [140]. © (2004) John Wiley & Sons Inc.)

The experimental work in this early report may have been restricted by the small range of attainable scan velocities and the limited number of data points. More recent work, in which among others the rigorous calibration of the LFM setup, an enhanced range of scan velocities without compromised noise and data resolution, and the control of all relevant experimental parameters have been implemented, confirm some of these early observations (see below).

Importantly, the paper by Hammerschmidt and co-workers successfully utilized a means to convert the scan velocities to frequencies by considering the tip–sample contact length [142, 143]. For temperatures below $T_g$ this approach can be applied to normalize the scan velocities by simple division of the velocity by this contact length. This approach also implies that the tip radius is a decisive factor in determining the *frequency* of the experiment for

constant experimental conditions (temperature, velocity etc.). In fact, by systematic variations in tip radius, a large range of frequencies can be covered with a given range of scan velocities. For comparisons with bulk data the knowledge of the corresponding frequencies is crucial.

As shown in Fig. 26, the friction force vs. velocity relationship assessed for a 125 nm thick PMMA film depends on the temperature of the experiment, as reported by Tocha, Schönherr and Vancso. In these experiments the applied normal forces were limited to $\leq 1$ nN to ensure that the surface of the film to a depth of $\leq 2$ nm was probed. In addition, care was taken to confirm the absence of ploughing. A clear maximum is observed that shifts to higher velocities with increasing temperature, in accordance with the time–temperature superposition principle (see also Fig. 2).

Data acquired with probes that possessed different tip radii showed a markedly different behavior. This is evident for selected data shown in Fig. 27, in which the data was converted to interfacial shear stress vs. frequency by considering the contact area (estimated according to the JKR model) and the contact length, respectively [46]. Before the conversion to frequency (data not shown), the data showed no consistent monotonic (or other behavior). Only after the mentioned transformation is it obvious that the data acquired with probes with widely different radii belong to different parts of the friction force–velocity phase space. From these data it becomes evident that a large range of frequencies from Hz to MHz was probed using tips with different radii. Low frequencies were accessed in experiments with large tip radii, whereas high frequencies were characterized using sharp probes.
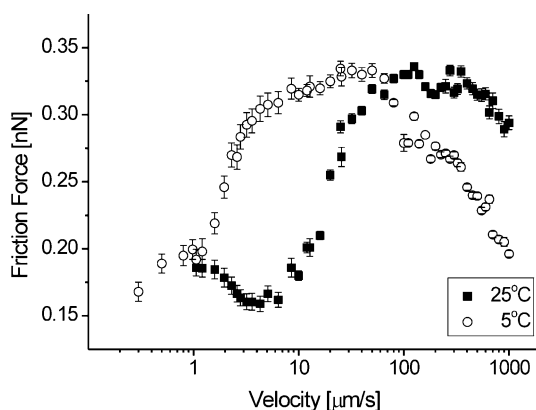


**Fig. 26**  Semi-log plot of friction force vs. velocity for PMMA film on oxidized silicon (thickness 125 nm) measured with an oxidized silicon tip ($R = 20$ nm) in nitrogen atmosphere (<5% RH) at various temperatures: 25 °C and 5 °C. A load of 0.2 nN was maintained constant during the measurements. The error bars indicate the standard deviation of the data analyzed for a given velocity ($n = 150$)

**Fig. 27** Effect of different tip radii on interfacial shear stress vs. frequency for PMMA film on oxidized silicon (thickness 125 nm) measured in nitrogen atmosphere (<5% RH) at 26 °C (tip radii: **a** 870 nm, **b** 150 nm, and **c** 20 nm). In **a**, **b**, and **c** loads of 2 nN, 2 nN, and 0.2 nN, respectively, were maintained constant during the measurements. The error bars indicate the standard dev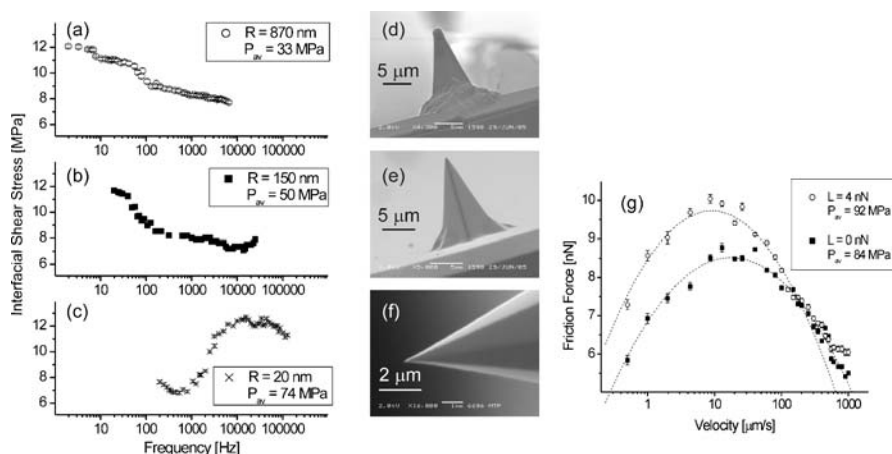iation of the data analyzed for a given velocity ($n = 150$). SEM images of the tips with radii (**d** $R = 870$ nm, **e** 150 nm, and **f** 20 nm). **g** Observed effect of different contact pressure on friction force vs. velocity for PMMA films on oxidized silicon (thickness 125 nm) measured with a $Si_3N_4$ tip ($R = 35$ nm) in nitrogen atmosphere (<5% RH) at 26 °C. The error bars indicate the standard deviation of the data ($n = 150$) analyzed for a given velocity. The transformation of velocity to frequency was performed using the procedure introduced in the previous section

In addition to these corrections, the effect of the different contact pressures (as a consequence of the different tip radii) on the measured relaxations must be accounted for (Fig. 27g). As shown, for increased load the peak observed was shifted horizontally to lower velocities. This observation is ascribed to the effect of the contact pressure exerted by the tip, which hinders locally the motion of the chain and rotation of the side groups (see below). Thus, the relaxation shifts to lower frequencies, which is similar to the effect observed with decreasing temperature (compare Fig. 2). The influence of pressure on the relaxation temperature was estimated from the value of the activation energy, assuming a value of 35 kJ mol$^{-1}$ (for a tip with 20 nm radius). The approximated increase of the relaxation temperature of 0.5 °C MPa$^{-1}$ is in good agreement with the effect of hydrostatic pressure ($\sim$0.35 °C MPa$^{-1}$) [41, 145]. Therefore, an increase as high as 20 °C can be expected for the same relaxation probed with the sharp tip ($R = 20$ nm), as compared to the large tip ($R = 870$ nm) at the same applied force.

The presence or absence of pressure induced shifts in LFM and related experiments has similar to the question of altered surface $T_g$'s been a controversial issue in the literature. Dinelli et al. argued that pressure-induced

changes in the determined $T_g$ can be excluded [146]. The local pressure applied by an LFM tip was thought to be insufficient to generate a pressure effect that results in an increase in the apparent $T_g$. In fact, at a constant velocity, the apparent $T_g$ was found to decrease and to approach the bulk value with increasing load. At a fixed load, the apparent $T_g$ was found to decrease, as expected, and to approach the bulk value with decreasing velocity. Dinelli et al. assigned the shift in $T_g$ to "the dynamic nature of the experiment" and not to an actual change in material property, as would be the case for a hydrostatic pressure. In addition, for very thin PS films (thickness 17–50 nm) no pressure effects were observed in SMFM measurements [147].

By contrast, an elevation in the apparent glass transition temperature for PS was reported by Schmidt et al. [148, 149]. This finding was attributed by the authors to a reduction of the free volume in the polymer due to large compressive stress beneath the sliding probe. Similarly, for PP, Gracias et al. reported a $T_g$ that was 20 °C higher for a sharp probe as compared to a large probe due to greater pressure, in accordance with PVT data [150]. In these experiments, the authors did not correct for changes in the contact length which in turn affect the velocity (see above).

Selected friction force vs. velocity master curves constructed from data obtained in experiments with tips with different radii are displayed in Fig. 28. The data were shifted according to the time–temperature superposition principle to a reference temperature of 26 °C to afford the corresponding activation energies. When compared to bulk relaxations, two relaxations can be distinguished: one of lower frequency (higher temperature) and one of higher frequency (lower temperature). These relaxations are attributed to the $\alpha$ and the $\beta$ processes in panels (b) and (a), respectively.

The observed peak in Fig. 28a is located in the MHz range, as is evident after the conversion of velocity to frequency (compare Fig. 27 and [144]) and
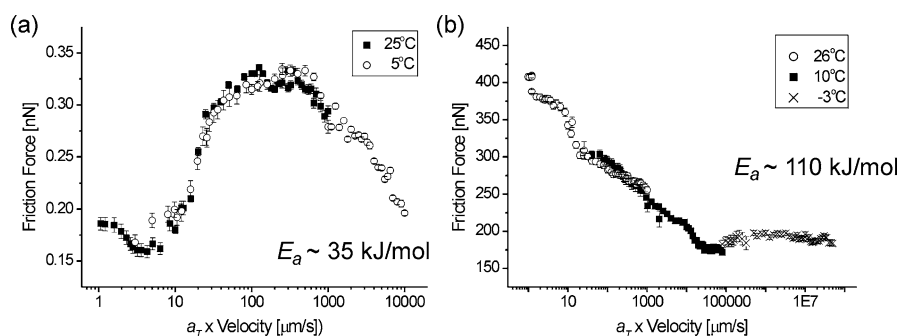


**Fig. 28** Masterplot constructed according to the time–temperature superposition principle of friction force vs. velocity for PMMA film on oxidized silicon (thickness 125 nm) measured **a** with an oxidized silicon tip ($R = 20$ nm) and **b** with an oxidized silicon tip ($R = 870$ nm) in nitrogen atmosphere (<5% RH) at various temperatures

was assigned to the $\beta$-relaxation of PMMA. This relaxation is the result of the rotation of the $-(CO)OCH_3$ side groups around the $C-C$ bonds linking the side groups to the main polymer chain [41]. The value of the corresponding activation energy of $\sim 35\,kJ\,mol^{-1}$ is significantly lower than the bulk value $(71-96\,kJ\,mol^{-1})$ determined by mechanical and dielectric methods [29]. Furthermore, the frequency of the $\beta$-relaxation is significantly higher $(10^6\,Hz)$ than the frequency detected in bulk measurements $(10-100\,Hz)$ at room temperature [144]. Both the higher frequency and lower activation energy indicate greater free volume and correspondingly higher mobility at the polymer surface.

The part of the relaxation curve detected at lower frequencies $(1-10^4\,Hz)$ is attributed to the $\alpha$-transition. From the changing slope of the curve, the maximum can be anticipated at around 1 Hz. The curve is expected to possess a bell shape. However, due to increasing ploughing and plastic deformation it was impossible to measure the bend at low velocities (frequencies). This additional component to friction force is known to change the shape of the relaxation curve [33]. In other LFM experiments published in the literature these effects have mostly not been appropriately taken into account.

The estimated activation energy of $110\,kJ\,mol^{-1}$ observed is significantly lower than the bulk value $(334-460\,kJ\,mol^{-1})$ and the relaxation frequency is noticeably higher compared to the bulk ($f = 1\,Hz$, $T = 26\,°C$ and $f = 1\,Hz$, $T = 100\,°C$, respectively) [29]. The overlap of curves characteristic for the $\alpha$ and $\beta$ relaxations was observed at a frequency of about $2 \times 10^4\,Hz$ at $26\,°C$ [144], which is noticeably lower in temperature in comparison with bulk mechanical studies ($f = 2 \times 10^4\,Hz$, $T = 50\,°C$) [29]. The determined activation energy of $60\,kJ\,mol^{-1}$ is influenced by both $\alpha$ and $\beta$ processes due to their different activation energies and shift factors. Thus, the resultant shift factor (activation energy) will be a superposition of $\alpha$ and $\beta$ processes. These observations of low activation energies and higher relaxation frequencies are consistent with the reported greater free volume at the polymer–air interface [151].

The combined approach of a high velocity actuator and control of tip–sample contact length allowed Tocha et al. to probe the $\alpha$ and the $\beta$ relaxations of PMMA at $26\,°C$, which is significantly below the bulk $T_g$ [144]. The central advantage of this method, as compared to the friction force studies carried out at variable temperature only, is that significant artifacts due to changes in the materials properties (Young's modulus, adhesion, scratch resistance) associated with the glass transition can be circumvented. For PMMA a fully consistent picture has thus emerged, in which significantly lowered activation barriers and increased frequencies coincide, as expected based on the time–temperature superposition principle.

Consistent with this interpretation is the report by Hammerschmidt et al. who studied the effect of water on the friction force measured, among other materials, on PVOH films. The friction data acquired at different scan veloci-

ties was converted to frequency as discussed above by dividing the velocity by the tip–sample contact diameter. Water was found to act as a plasticizer for PVOH, as expected. The temperature at which a particular relaxation occurred was lowered with increasing water content, which is equivalent to decreasing relaxation times [143].

Deviations from behavior that would be expected on the basis of the time–temperature superposition principle were attributed to triboheating effects. The energy dissipated in the contact between tip and sample was assumed to locally increase the temperature, which explains the observed decrease in friction force with increasing scan size ($0.2$–$150\,\mu$m) for the scan rates less than $\sim 500\,\mu\mathrm{m\,s^{-1}}$ in LFM measurements on gelatin films. It was further demonstrated that the heating effect could cause position shifts in a friction peak (which was presumed to be the glass transition of the gelatin film) [152].

Similarly, in PtBuA, the friction vs. velocity peak observed in LFM experiments was found to shift towards higher scan rates as the external load was increased. Similar friction peaks shifted to the low-temperature side when the external load was increased or the scan size decreased. In all cases, the observed shifts in the friction peak are consistent with an effect from heating [153].

## 3.3
## Thin Films and Confinement Effects

As mentioned in Sects. 1 and Sect. 3.2, polymer relaxations can be affected by confinement effects and the presence of interfaces. Depressed or elevated $T_g$'s in ultrathin films exemplify this effect [10, 11]. In addition, it has been reported, for instance, that the structural, material, and transport properties become increasingly dominated by interfacial, conformational, and dimensional constrains, when the thickness is reduced to the sub-100 nm scale [146, 154, 164]. For such ultrathin films, depending on the thickness, crystallization kinetics and degree of crystallinity [8, 155, 156], phase behavior [157–159], morphology [160], permeability [7], or dewetting [9] may be altered, among other properties.

The interface of polymer films with vacuum or air results according to Torkelson and coworkers in increased mobility at this interface [128]. The depth to which this effect can be detected inside the film depends on nanoconfinement, as elucidated in detailed fluorescence spectroscopy studies with layered polymer thin films systems. AFM measurements have also provided novel insight into thin film and confinement effects, i.e. to unravel how far the behavior of polymers is changed when polymer chains reside for instance near interfaces or are confined in ultrathin films.

In a detailed study on the effect of film thickness on the glass transition temperature, Fryer et al. acquired data with scanning thermal probe microscopy and compared these with ellipsometry measurements. The ad-

vantage of using different methods is obvious since changes in complementary properties are being detected. In ellipsometry the thermal expansion of the film is assessed, while scanning thermal probe microscopy probes e.g. the change in film modulus via the cantilever deflection induced by the thermal probe [161]. As shown in Fig. 29, the cantilever deflects markedly when the PS film softens, hence the onset of the $T_g$ can be assessed [161].

In Fig. 30, two different scenarios are compared: PS (left) and PMMA (right) on $SiO_2$ and hydrophobized $SiO_2$. For film thicknesses below $\sim$50 nm an altered $T_g$ was detected. In accordance with the ellipsometry data (and reported literature data), non-interacting surfaces and interacting surfaces led to the depression and the increase in $T_g$, respectively.
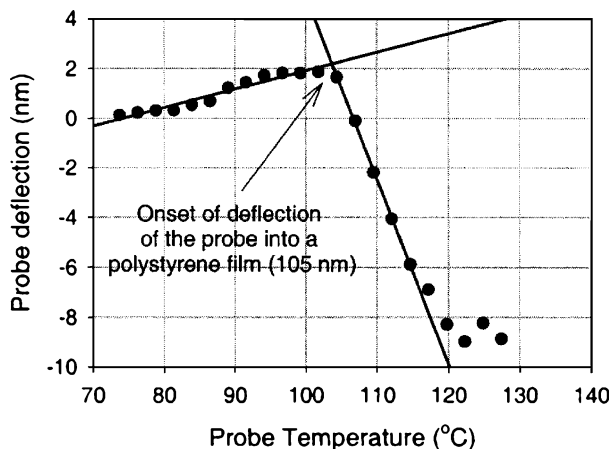


**Fig. 29** Plot of the thermal probe deflection vs. temperature measured on a 105 nm thick film of PS on a hydrophobized substrate. (Reproduced with permission from [161]. © (2000) American Chemical Society)
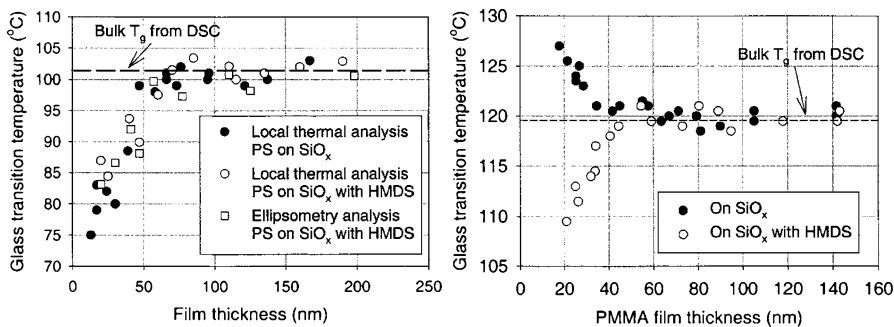


**Fig. 30** Values of $T_g$ determined for PS (*left*) and PMMA (*right*) ultrathin films on various substrates. (Reprinted with permission from [161]. © (2000) American Chemical Society)

The group of Kajiyama reported, as already mentioned in Sect. 3.2, indications of a lowered $T_g$ at the film surface. In LFM experiments, a lateral force peak corresponding to the surface $\alpha$-relaxation process of segmental motion was observed at a temperature much lower than the bulk $T_g$. For thinner films (3–4 the radius of gyration of the unperturbed chain) the peak on the lateral force vs. temperature curve broadened out with decreasing film thickness and eventually split into two peaks. The $T_g$ determined was independent of the film thickness. On the other hand, the apparent activation energy was altered [162].

By contrast, Ge et al. observed by SMFM for PS films with a thickness between 17 and 500 nm that the value of $T_g$ is equal to the bulk value and is independent of the film thickness for thicknesses exceeding 17 nm. In addition, the strength of the substrate-polymer interactions was shown to play no role. Even a free standing film on a 10 μm hole did not show a different $T_g$ according to these data [147], even though ellipsometry data on free-standing films suggested substantial depressions [163].

Overney and coworkers investigated PS films on hydrogen passivated Si, as well as on OTS and PVP coated Si. These latter surfaces were chosen as model surfaces for low interaction interfaces. The reported LFM and shear modulation mode AFM data suggested that $T_g$ for thick films corresponds to the bulk value. However, for film thickness below 200 nm, confinement effects due to the close substrate and the film preparation technique can significantly alter the phase of polymer. For films thinner than 150 nm, $T_g$ was found to be elevated. Below 20 nm, no $T_g$ was found. For low interaction interfaces, PS on PVP and OTS, $T_g$ was independent of film thickness [164]. As shown in Fig. 31 (left), the friction force measured at constant load decreased when the film thickness is less than a critical thickness $t_{c1}$. The adhesive forces (data not shown here) did not depend on film thickness. The authors show that
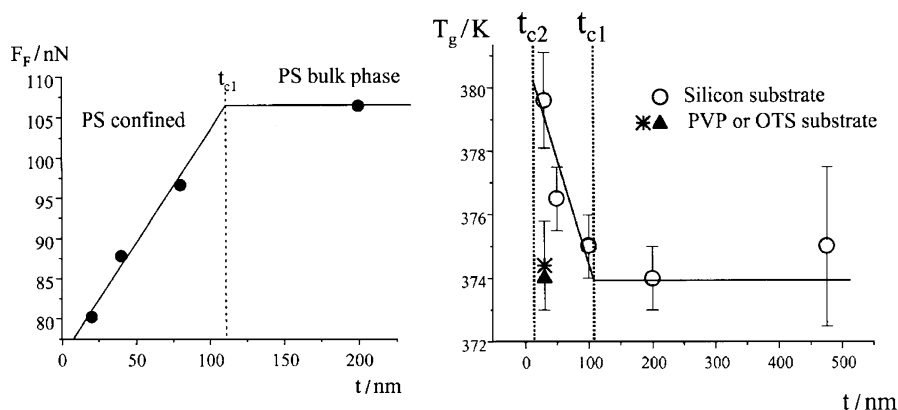


**Fig. 31** Values of friction force (*left*) and $T_g$ (*right*) vs. film thickness determined for PS on various substrates. (Reproduced with kind permission of Springer Science and Business Media from [164]. © (2000) Kluwer Academic Publishers)

such a decrease in friction goes along with an increase in the elastic modulus, i.e. the PS film is constrained within a boundary regime of thickness $t_{c1}$ towards the substrate surface. For films with a thickness between $t_{c1}$ and $t_{c2}$ (boundary regime) the glass transition was found to be elevated (Fig. 31, right). Below $t_{c2}$ no glass transition was detected (sublayer regime).

Another example of interfacial confining effects, observed for spin-coated films of PnBMA was reported by these authors (Fig. 32). For film thicknesses below 50 nm the $T_g$ was found to be elevated.

These data were rationalized by the occurrence of an increased lateral disentanglement of polymer chains that is caused during the spin-coating process. Temperature-driven annealing was deemed to be not successful in the case of interactive interfaces. Thus, the heterogeneous structure is established normal to the substrate and effectively creates a property gradient in the polymer matrix. For films with a thickness below 150 nm, the $T_g$ increases with decreasing distance to the substrate interface, while for thicknesses of 20 nm and less a transition is no longer observable.

Work by Wang and Ishida on PVME (thickness 5–400 nm) employing LFM and adhesion measurements as a function of scanning rate and film thickness also demonstrated confinement effects. When the film thickness falls below 200 nm, the lateral force of the PVME films decreases with decreasing film thickness, consistent with the data by Overney et al. on PS (see above), and becomes less dependent on the scanning rate. Local adhesion measurements indicate that the adhesion force per unit area increases with the decreasing film thickness. These results are consistent with each other and point to an increased polymer stiffness and decreased polymer chain mobility due to the confinement in the ultra-thin films [165].
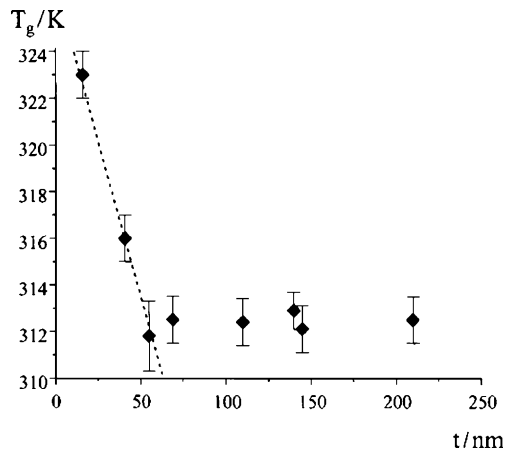


**Fig. 32** Values of $T_g$ vs. film thickness determined for poly(*n*-butyl methacrylate). (Reproduced with kind permission of Springer Science and Business Media from [164]. © (2000) Kluwer Academic Publishers)

For PtBuA (thickness 10–133 nm) Wang et al. reported negligible differences in the dynamic behavior between the bulk and the free surface of ultrathin films $d > 15$ nm. These authors analyzed $f$–$d$ curves acquired at different temperatures and different probe rates. The adhesion master curves and shift factors thus obtained showed no dependence on the film thickness. However, for $d < 15$ nm samples, a suppression in shift factors was found that becomes more pronounced as $d$ decreases. These data are consistent with the existence of an immobile component in the layer of polymer next to the substrate wall and long-range effects from the substrate that influence the surface segmental mobility [166].

These different reports clearly show that the range of the effects mentioned may differ depending on the interaction of the polymer with the substrate, the overall film thickness, but also the sample history and chain entanglements.

## 3.4
## Anisotropy of Friction and Different Wear Modes and Tribological Behavior

Many examples in the literature show that plastic deformation even of glassy polymers, such as polystyrene, may occur under relatively modest loads in CM-AFM experiments. As summarized in Fig. 33, the formation of more or less regularly spaced ridges perpendicular to the fast scan direction is observed in a typical contact mode AFM scan (here the slow scan axis was disabled). The amplitude of the ridges increases over time (from top to bottom) and it is obvious that instead of analyzing the underlying amorphous polymer, the surface is being modified by the scanning AFM tip [167].

The time–temperature dependence of the patterns is well described by the WLF equation, which is typically used to describe viscoelastic behavior of polymers. The detailed analysis of the data further suggested an increased $T_g$
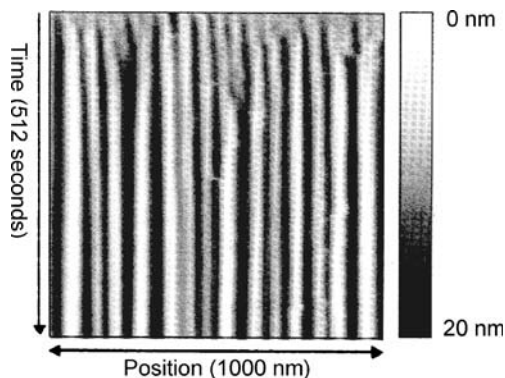
**Fig. 33** Formation of parallel ridges on PS imaged by CM-AFM under a load of 30 nN. The slow scan axis (down scan) was disabled hence the vertical axis corresponds to time. (Reprinted from [167] with permission from Elsevier. © (1999) Elsevier)

derived from elevated pressure beneath the tip [8]. As alluded to in previous sections, the onset of plastic deformation may complicate the analysis of friction forces as ploughing terms need to be considered in addition to interfacial friction.

On the molecular level, stick-slip motion has been observed, similar to atomic-scale stick slip on e.g. mica [168] and graphite [169]. An illustrative example of molecular stick slip for polymers has been reported for friction forces measured on PTFE [170, 171]. As shown in Fig. 34, the stick-slip motion corresponds to the molecular corrugations of the PTFE chains. Similar observations have been reported for polyethylene [172]. For such extended-chain crystals maximum friction was observed perpendicular to and minimum friction for scan parallel to the chain direction, respectively. This friction anisotropy can be rationalized in terms of the cobblestone model (interlocking asperity model) of interfacial friction described e.g. by Israelachvili and coworkers [173, 174].

The tip–sample frictional interaction as measured by AFM may also depend upon the molecular/atomic orientation and structure of the interface in a measurable fashion for materials other than atomically smooth atomic or molecular crystals [175, 176]. An impressive example of friction anisotropy was found for a thiolipid monolayer on mica by Liley et al. [177]. These authors observed a flower-shaped structure, formed by domains with different molecular orientation. The dependence of friction force on scanning direction suggested that molecules possess a radial tilt, which is directed towards the center of the "flower".
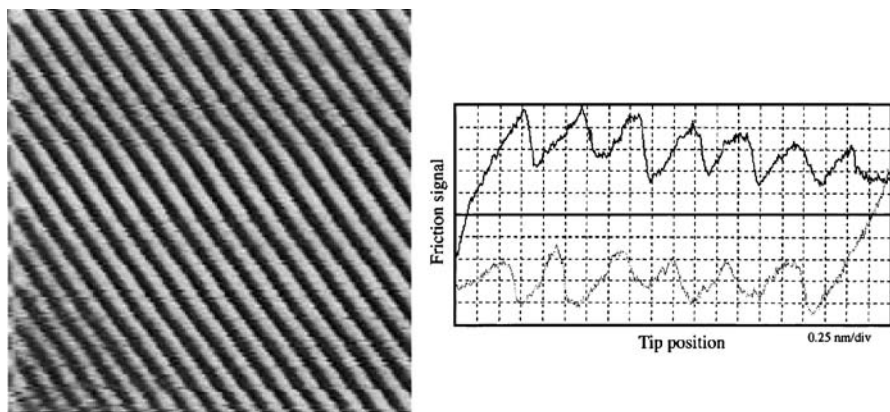


**Fig. 34** *Left*: lateral force microscopy image of PTFE deposited on muscovite mica showing molecular resolution. Scan size: 10.7 nm×10.7 nm; (scan direction: 55° with respect to the chain direction); *right*: a typical LFM scope trace showing a friction loop. Scanning proceeds from left to right on the *top line* (trace) and from *right* to *left* following the *bottom line* (retrace). Scanning was performed at 66.3° with respect to the chain direction. (Reprinted with permission from [170]. © (1996) American Chemical Society)
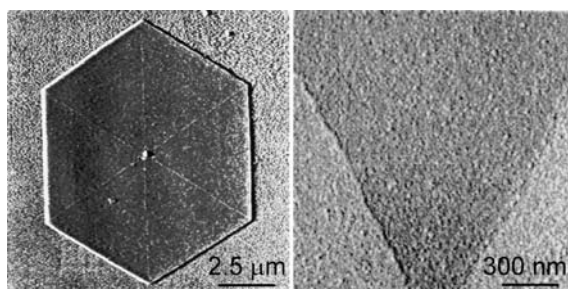
**Fig. 35** Lamellar crystals of poly(oxymethylene) with clearly resolved chain fold domains at the surface of the lamellae defined by the diagonals and the edges of the crystals. The frictional force within the domains, obtained in AFM experiments, was found to depend on the relative scan direction. (Reprinted from [180] with permission from Elsevier. © (1994) Elsevier)
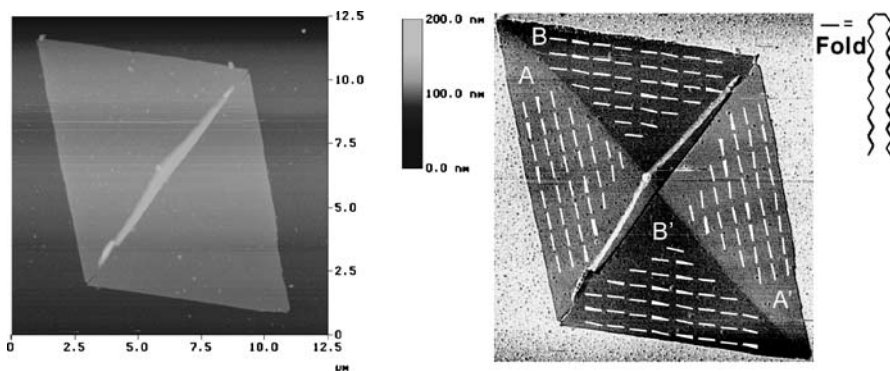


**Fig. 36** *Left*: height image of a collapsed PE lamella; *right*: friction image of the same PE crystal including schematic drawing of fold direction. (Reprinted with permission from [174]. © (1999) American Chemical Society)

For polymers anisotropic friction was in particular unveiled at the surface of lamellar polymer crystals (see Figs. 35 and 36), including poly(oxymethylene) [174, 178] and polyethylene [174, 179, 180], as well as on oriented PTFE and PE films [170, 174]. The anisotropic friction for lamellar crystals is explained by the occurrence of chain-folding oriented preferentially in planes parallel to the corresponding growing crystal face.

# 4
# Outlook

The recent results and reports in the area of friction of polymers and its relation to polymer chain dynamics and relaxations, as reviewed above, do

not only show the renewed interest in important fundamental aspects of polymer science, but reflect the challenges met and to be addressed in current and future technology. This refers in particular to (ultra)thin polymer films and coatings, as well as polymer-based devices and processes with submicrometer to nanoscale dimensions. As alluded to throughout this article, interfacial and confinement effects play an increasingly important role on these length scales. These may become determining factors that are critical for reliable device performance or error-free fabrication processes, hence the corresponding effects and phenomena become part of the engineering of polymer materials in these areas.

It is thus fair to conclude that precise material engineering with polymers on the nanoscale is only possible with an understanding of the polymer dynamics near interfaces. Hence, the characterization and control of thin films and interfacial boundary layers become vitally important for nanotechnological applications, such as nano-electromechanical systems (NEMS) for terabit thermomechanical storage, protective coatings, adhesives and lubricants that rely on very specific relaxation and transition properties in sub-100 nm systems [23, 24, 181]. As shown, the widespread application of proximal scanning probe methods also underlines the importance of (local) probing of (macro)molecular dynamics, e.g. near the glass transition.

The recent significant progress regarding the instrumental and technical sophistication of these measurements, including truly quantitative measurements and analyses of the acquired data, controlled tip–sample interactions, and the realization of a broad range of temperatures and scan rates (also considering the relation of tip radius and actual frequencies) promise rapidly progressing insight. These developments are and will be complemented by implementing increasingly realistic experimental conditions (to be able to relate nanoscale and macroscale tribology for instance), including, for example, controlled chemistry (tribochemistry) and controlled media.

Similarly important are advances and progress in modeling and simulations, which are not within the scope of this review. In general, complementary AFM experiments and molecular dynamics (MD) simulations now facilitate the study of contact areas of similar dimensions (since MD recently increased the number of atoms or molecules involved in the contact), but still differ drastically in the time scale of the measurements. MD simulations are currently limited to timescales no greater than tens of nanoseconds and length scales of tens of nanometers, which are insufficient for analyzing many tribological systems [182]. Similarly, a gap can be identified between molecular or atomistic models on the one hand, and continuum (e.g. contact mechanics) approaches that describe the deformation between elastic single asperities on the other hand. Consequently, fundamental aspects of friction and the mechanisms of energy dissipation are poorly understood on a first-principles level. Multi-level experiments (from micrometer to nanometer scale) are clearly required to advance the understanding of tribology.

Work on the necessary bridge between micro- and nanotribology, as well as atomistic and continuum models has only recently begun to emerge.

It is beyond doubt that the mentioned combination of experiment and theory is critically important to reach any of the targets and aims named above. The problem of bridging the gap of length and time scales thus not only refers to AFM-type approaches in relation to polymer dynamics and friction, but also refers to simulations and the development of a congruent picture that encompasses both experimental and theoretical results.

# References

1. Bhushan B (ed) (1999) Handbook of Micro/Nano Tribology. CRC Press, New York, p 371
2. Meyer E, Overney RM, Dransfeld K, Gyalog T (1998) Nanoscience: Friction and Rheology on the Nanometer Scale. World Scientific, Singapore
3. Williams ML, Landel RF, Ferry JD (1955) J Am Chem Soc 77:3701
4. Kato T, Kawaguchi M, Sajjad MM, Choi J (2004) Wear 257:909
5. Soles CL, Lin EK, Lenhart JL, Jones RL, Wu WL, Goldfarb DL, Angelopoulos M (2001) J Vac Sci Techn B 19:2690
6. Alcoutlabi M, McKenna GB (2005) J Phys Cond Matter 17:R461
7. Pfromm PH, Koros WJ (1995) Polymer 36:2379
8. Despotopoulou MM, Frank CW, Miller RD, Rabolt JF (1996) Macromolecules 29:5797
9. Reiter G (1993) Europhys Lett 23:579
10. Keddie JL, Jones RAL, Cory RA (1994) Europhys Lett 27:59
11. Forrest JA, DalnokiVeress K, Stevens JR, Dutcher JR (1996) Phys Rev Lett 77:2002
12. Roth CB, McNerny KL, Jager WF, Torkelson JM (2007) Macromolecules 40:2568
13. Jones RAL, Richards RW (1999) Polymers at Surface and Interfaces. Cambridge University Press, Cambridge, UK
14. Sillescu H (1999) J Non-Crystalline Solids 243:81
15. McClelland GM, Glosli JN (1992) In: Singer IL, Pollock HM (eds) Fundamentals of Friction: Macroscopic and Microscopic Processes. Kluwer, Dordrecht, p 405
16. Colchero J, Meyer E, Marti O (1999) In: Bhushan B (ed) Handbook of Micro/Nano Tribology. CRC Press, New York, p 273
17. Johnson KL (1985) Contact Mechanics. Cambridge University Press, Cambridge
18. Carpick RW, Ogletree DF, Salmeron MJ (1999) Coll Interf Sci 211:395
19. Binnig G, Quate CF, Gerber C (1986) Phys Rev Lett 56:930
20. Colton R J, Engel A, Frommer J E, Gaub H E, Gewirth A A, Guckenberger R, Rabe J, Heckl W M, Parkinson B (1998) Procedures in Scanning Probe Microscopies. Wiley, New York
21. Carpick RW, Salmeron M (1997) Chem Rev 97:1163
22. Ferry JD (1980) Viscoelastic Properties of Polymers. Wiley, New York
23. Lutwyche MI, Despont M, Drechsler U, Dürig U, Häberle W, Rothuizen H, Stutz R, Widmer R, Binnig GK, Vettiger P (2000) Appl Phys Lett 77:3299

24. Dürig U, Cross G, Despont M, Drechsler U, Häberle W, Lutwyche MI, Rothuizen H, Stutz R, Widmer R, Vettiger P, Binnig GK, King WP, Goodson KE (2000) Tribol Lett 9:25
25. Cagin T, Che JW, Gardos MN, Fijany A, Goddard WA (1999) Nanotechnology 10:278
26. Granick S, Lin Z, Bae SC (2003) Nature 425:467
27. Flory PJ (1969) Statistical Mechanics of Chain Molecules. Interscience Publishers, New York
28. Sperling LH (1985) Introduction to Physical Polymer Science. Wiley, New York
29. McCrum NG, Read BE, Williams G (1967) Anelastic and Dielectric Effects in Polymeric Solids. Wiley, London
30. Hammerschmidt JA, Gladfelter WL, Haugstad G (1999) Macromolecules 32:3360
31. Young RJ, Lovell PA (1991) Introduction to Polymers. Chapman & Hall, London
32. Cherry BW (1981) Polymer Surfaces. Cambridge University Press, Cambridge
33. Grosch KA (1963) Proc R Soc London Ser A—Math Phys Sci 274:21
34. Ardi MS, Dick W, Kubat J (1993) Coll Polym Sci 271:739
35. Bergman R, Alvarez F, Alegria A, Colmenero JJ (1998) Chem Phys 109:7546
36. Sane SB, Knauss WG (2001) Mech Time-Depend Mater 5:293
37. Sane SB, Knauss WG (2001) Mech Time-Depend Mater 5:325
38. de Deus JF, Souza GP, Corradini WA, Atvars TDZ, Akcelrud L (2004) Macromolecules 37:6938
39. Schmidt-Rohr K, Kulik AS, Beckham HW, Ohlemacher A, Pawelzik U, Boeffel C, Spiess W (1994) Macromolecules 27:4733
40. Dubek G, Lupke T, Stejny J, Alam MA, Arnold M (2000) Macromolecules 33:990
41. Gedde UW (1999) Polymer Physics. Kluwer Academic Publishers, Dordrecht
42. Israelachvili JN, Berman AD (1999) In: Bhushan B (ed) Handbook of Micro/Nano Tribology. CRC Press, New York, p 371
43. Homola AM, Israelachvili JN, McGuiggan PM, Gee ML (1990) Wear 136:65
44. Bowden FP, Tabor D (1966) Brit J Appl Phys 17:1521
45. Hertz HJ (1882) Reine Angew Math 92:156
46. Johnson KL (1997) Proc R Soc London Ser A—Math Phys Eng Sci 453:163
47. Johnson KL (1996) Langmuir 12:4510
48. Muller V, Derjaguin BV, Toporov YP (1983) Coll Surf 7:251
49. Derjaguin BV, Muller V, Toporov YP (1980) J Coll Interf Sci 73:293
50. Derjaguin BV, Muller V, Toporov YP (1978) J Coll Interf Sci 67:378
51. Derjaguin BV, Muller V, Toporov YP (1978) J Coll Interf Sci 53:314
52. Maugis DJ (1992) Coll Interf Sci 150:243
53. Tabor DJ (1977) Coll Interf Sci 58:2
54. Schwarz UD (2003) J Coll Interf Sci 261:99
55. Johnson KL (1999) In: Tsukruk VV, Wahl KJ (eds) Microstructure and Microtribology of Polymer Surfaces. ACS Symp Ser Vol 741. American Chemical Society, Washington, p 24
56. Giri M, Bousfield DB, Unertl WN (2001) Langmuir 17:2973
57. Hui CY, Baney JM, Kramer EJ (1998) Langmuir 14:6570
58. Lin YY, Hui CY, Baney JM (1999) J Phys D Appl Phys 32:2250
59. Lin YY, Hui CY (2002) J Polym Sci B-Polym Phys 40:772
60. Greenwood JA, Williamson JB (1966) P Proc R Soc London A 295:300
61. Greenwood JA, Tripp JH (1967) Trans ASME Ser E, J Appl Mech 34:153
62. Greenwood JA (1967) Trans ASME Ser F, J Lubrication Technol 89:81
63. Overney R, Meyer E (1993) MRS Bull 18:26
64. Liu YH, Wu T, Evans DF (1994) Langmuir 10:2241

65. Perry SS (2004) MRS Bull 29:478
66. Meyer G, Amer NM (1990) Appl Phys Lett 57:2089
67. Binggeli M, Christoph R, Hintermann HE (1995) Tribol Lett 1:13
68. Schwarz UD, Köster P, Wiesendanger R (1996) Rev Sci Instrum 67:2560
69. Warmack RJ, Zheng XY, Thundat T, Allison DP (1994) Rev Sci Instrum 65:394
70. Proksch R, Schaffer TE, Cleveland JP, Callahan RC, Viani MB (2004) Nanotechnology 15:1344
71. D'Costa NP, Hoh JH (1995) Rev Sci Instrum 66:5096
72. Gibson CT, Watson GS, Myhra S (1997) Wear 213:72
73. Burnham NA, Chen X, Hodges CS, Matei GA, Thoreson EJ, Roberts CJ, Davies MC, Tendler SJB (2003) Nanotechnology 14:1
74. Landau LD, Lifshitz EM (1986) Theory of Elasticity, vol 7. Pergamon Press, Oxford
75. Albrecht TR, Akamine S, Carver TE, Quate CF (1990) J Vac Sci Technol A—Vac Surf Films 8:3386
76. Sader JE (1995) Rev Sci Instr 66:4583
77. Wortman JJ, Evans RA (1965) J Appl Phys 36:153
78. Noy A, Frisbie CD, Rozsnyai LF, Wrighton MS, Lieber CM (1995) J Am Chem Soc 117:7943
79. Kiesewetter L, Zhang JM, Houdeau D, Steckenborn A (1992) Sens Actuator A—Phys 35:153
80. Schneider D, Tucker MD (1996) Thin Solid Films 291:305
81. Levy R, Maaloum M (2002) Nanotechnology 13:33
82. Ma HL, Jimenez J, Rajagopalan R (2000) Langmuir 16:2254
83. Butt HJ, Jaschke M (1995) Nanotechnology 6:1
84. Tortonese M, Kirk M (1997) Proc SPIE 3009:53
85. Cleveland JP, Manne S, Bocek D, Hansma PK (1993) Rev Sci Instrum 64:403
86. Buenviaje CK, Ge SR, Rafailovich MH, Overney RM (1998) Mat Res Soc Symp Proc 522:187
87. Liu E, Blanpain B, Celis JP (1996) Wear 192:141
88. Feiler A, Attard P, Larson I (2000) Rev Sci Instrum 71:2746
89. Ogletree DF, Carpick RW, Salmeron M (1996) Rev Sci Instrum 67:3298
90. Varenberg M, Etsion I, Halperin G (2003) Rev Sci Instrum 74:3362
91. Tocha E, Schönherr H, Vancso GJ (2006) Langmuir 22:2340
92. Tocha E, Stefański T, Schönherr H, Vancso GJ (2005) Rev Sci Instrum 76:083704
93. Lubben JF, Johannsmann D (2004) Langmuir 20:3698
94. Mindlin RD (1949) J Appl Mech 16:259
95. Pietrement O, Beaudoin JL, Troyon M (1999) Tibol Lett 7:213
96. Sills S, Overney RM (2006) In: Bhushan B, Fuchs H (eds) Applied Scanning Probe Methods III. Springer, Berlin Heidelberg New York, p 83
97. Kajiyama T, Tanaka K, Ohki I, Ge SR, Yoon JS, Takahara A (1994) Macromolecules 27:7932
98. Maivald P, Butt H-J, Gould SAC, Prater CB, Drake B, Gurley JA, Elings VB, Hansma PK (1991) Nanotechnology 2:103
99. Chi L-F, Anders M, Fuchs H, Johnston RR, Ringsdorf H (1993) Science 259:213
100. Chen JT, Thomas EL (1996) J Mater Sci 31:2531
101. Anczykowski B, Krüger D, Babcock KL, Fuchs H (1996) Ultramicroscopy 66:251
102. Jourdan JS, Cruchon-Dupeyrat SJ, Huan Y, Kuo PK, Liu G-Y (1999) Langmuir 15:6495
103. Burnham NA, Kulik AJ, Gremaud G, Gallo P-J, Oulevey F (1996) J Vac Sci Technol B 14:794

104. Huang L, Su CM (2004) Ultramicroscopy 100:277
105. Song YX, Bhushan B (2005) J Appl Phys 97:083533
106. Reinstadtler M, Kasai T, Rabe U, Bhushan B, Arnold W (2005) J Phys D, Appl Phys R269
107. Cappella B, Dietler G (1999) Surf Sci Rep 34:1
108. Butt H-J, Cappella B, Kappl M (2005) Surf Sci Rep 59:1
109. Tsui OKC, Wang XP, Ho JYL, Ng TK, Xiao X (2000) Macromolecules 33:4198
110. Cappella B, Kaliappan SK, Sturm H (2005) Macromolecules 38:1874
111. Binnig G, Despont M, Drechsler U, Haberle W, Lutwyche M, Vettiger P, Mamin HJ, Chui BW, Kenny TW (1999) Appl Phys Lett 74:1329
112. King WP, Kenny TW, Goodson KE, Cross G, Despont M, Durig U, Rothuizen H, Binnig GK, Vettiger P (2001) Appl Phys Lett 78:1300
113. Fischer H (2005) Macromolecules 38:844
114. Garcia R, Perez R (2002) Surf Sci Rep 47:197
115. Noy A, Vezenov DV, Lieber CM (1997) Annu Rev Mater Sci 27:381
116. Vancso GJ, Hillborg H, Schönherr H (2005) Adv Polym Sci 182:55
117. Sinniah SK, Steel AB, Miller CJ, ReuttRobey JE (1996) J Am Chem Soc 118:8925
118. Feldman K, Tervoort T, Smith P, Spencer ND (1998) Langmuir 14:372
119. Werts MPL, Van der Vegte EW, Grayer V, Esselink E, Tsitsilianis C, Hadziioannou G (1998) Adv Mater 10:452
120. Lee WK (1999) Polymer 40:5631
121. Cappella B, Kaliappan SK (2006) Macromolecules 39:9243
122. Satomi N, Tanaka K, Takahara A, Kajiyama T (2001) Macromolecules 34:6420
123. Nysten B, Legras R, Costa J-L (1995) J Appl Phys 78:5953
124. Tomasetti E, Nysten B, Legras R (1998) Nanotechnology 9:305
125. Nysten B, Meerman C, Tomasetti E (1999) In: Tsukruk VV, Wahl KJ (eds) Microstructure and Microtribology of Polymer Surfaces. ACS Symp Ser Vol 741. American Chemical Society, Washington, p 304
126. Cuberes MT, Assender HE, Briggs GAD, Kolosov OV (2000) J Phys D, Appl Phys 33:2347
127. Oulevey F, Burnham NA, Gremaud G, Kulik AJ, Pollock HM, Hammiche A, Reading M, Song M, Hourston DJ (2000) Polymer 41:3087
128. Ellison CJ, Torkelson JM (2003) Nature Mater 2:695
129. Priestley RD, Ellison CJ, Broadbelt LJ, Torkelson JM (2005) Science 309:456
130. Tomczak N, Vallee RAL, van Dijk EMHP, Kuipers L, van Hulst NF, Vancso GJ (2004) J Am Chem Soc 126:4748
131. Pu Y, Ge SR, Rafailovich M, Sokolov J, Duan Y, Pearce E, Zaitsev V, Schwarz S (2001) Langmuir 17:5865
132. Sills S, Gray T, Overney RM (2005) J Chem Phys 123:134902
133. Sills S, Overney RM (2003) Phys Rev Lett 91:095501
134. Kaliappan SK, Cappella B (2005) Polymer 46:11416
135. Bliznyuk VN, Assender HE, Briggs GAD (2002) Macromolecules 35:6613
136. Tanaka K, Takahara A, Kajiyama T (1997) Macromolecules 30:6626
137. Kajiyama T, Tanaka K, Takahara A (1997) Macromolecules 30:280
138. Kajiyama T, Tanaka K, Takahara A (1998) Polymer 39:4665
139. Satomi N, Tanaka K, Takahara A, Kajiyama T, Ishizone T, Nakahama S (2001) Macromolecules 34:8761
140. Kajiyama T, Tanaka K, Takahara A (2004) J Polym Sci Polym Chem 42:639
141. Tanaka K, Hashimoto K, Kajiyama T, Takahara A (2003) Langmuir 19:6573
142. Briscoe B, Smith AC (1982) J Phys D: Appl Phys 15:579

143. Hammerschmidt JA, Moasser B, Gladfelter WL, Haugstad G, Jones RR (1996) Macromolecules 29:8996
144. Tocha E, Schönherr H, Vancso GJ (2007) (submitted)
145. Schmidt M, Maurer FHJ (2000) Macromolecules 33:3879
146. Dinelli F, Buenviaje C, Overney RM (2000) J Chem Phys 113:2043
147. Ge S, Pu Y, Zhang W, Rafailovich M, Sokolov J, Buenviaje C, Buckmaster R, Overney RM (2000) Phys Rev Lett 85:2340
148. Schmidt RH, Haugstad G, Gladfelter WL (2003) Langmuir 19:10390
149. Schmidt RH, Haugstad G, Gladfelter WL (1999) Langmuir 15:317
150. Gracias DH, Zhang D, Lianos L, Ibach W, Shen YR, Somorjai GA (1999) Chem Phys 245:277
151. Mansfield KF, Theodorou DN (1991) Macromolecules 24:6283
152. Haugstad G, Gladfelter WL, Weberg EB, Weberg RT, Jones RR (1995) Langmuir 11:3473
153. Wang XP, Tsui OKC, Xiao XD (2002) Langmuir 18:7066
154. Sills S, Overney RM, Chau W, Lee VY, Miller RD, Frommer J (2004) J Chem Phys 120:5334
155. Sutton SJ, Izumi K, Miyaji H, Miyamoto Y, Miyashita S (1997) J Mater Sci 32:5621
156. Schönherr H, Frank CW (2003) Macromolecules 36:1199
157. Meuse CW, Yang XZ, Yang DC, Hsu SL (1992) Macromolecules 25:925
158. Tao HJ, Meuse CW, Yang XZ, Macknight WJ, Hsu SL (1994) Macromolecules 27:7146
159. Krausch G, Dai CA, Kramer EJ, Marko JF, Bates FS (1993) Macromolecules 26:5566
160. Fasolka MJ, Banerjee P, Mayes AM, Pickett G, Balazs AC (2000) Macromolecules 33:5702
161. Fryer DS, Nealey PF, de Pablo JJ (2000) Macromolecules 33:6439
162. Akabori K, Tanaka K, Kajiyama T, Takahara A (2003) Macromolecules 36:4937
163. Forrest JA, DalnokiVeress K, Dutcher JR (1997) Phys Rev E 56:5705
164. Overney RM, Buenviaje C, Luginbuhl R, Dinelli F (2000) J Therm Anal 59:205
165. Wang D, Ishida H (2006) CR Chimie 9:90
166. Wang XP, Xiao XD, Tsui OKC (2001) Macromolecules 34:4180
167. Pickering JP, Vancso GJ (1999) Appl Surf Sci 148:147
168. Hirano M, Shinjo K (1993) Wear 168:121
169. Sasaki N, Tsukada M, Fujisawa S, Sugawara Y, Morita S, Kobayashi K (1998) Phys Rev B 57:3785
170. Vancso GJ, Förster S, Leist H (1996) Macromolecules 29:2158
171. Vancso GJ, Förster S, Leist H, Liu G, Trifonova D (1996) Trib Lett 2:231
172. Schönherr H, Vancso GJ (1997) Macromolecules 30:6391
173. Israelachvili JN, Chen Y-L, Yoshizawa H (1995) In: Rimai DS, DeMejo LP, Mittal KL (eds) Fundamentals of Adhesion and Interfaces. VSP, Utrecht, p 261
174. Vancso GJ, Schönherr H (1999) In: Tsukruk VV, Wahl KJ (eds) Microstructure and Microtribology of Polymer Surfaces. ACS Symp Ser Vol 741. American Chemical Society, Washington, p 317
175. Overney RM, Takano H, Fujihira M, Paulus W, Ringsdorf H (1994) Phys Rev Lett 72:3546
176. Schönherr H, Kenis PJA, Engbersen JFJ, Harkema S, Hulst R, Reinhoudt DN, Vancso GJ (1998) Langmuir 14:2801
177. Liley M, Gourdon D, Stamou D, Meseth U, Fischer TM, Lautz C, Stahlberg H, Vogel H, Burnham NA, Duschl C (1998) Science 280:273
178. Nisman R, Smith P, Vancso GJ (1994) Langmuir 10:1667
179. Smith PF, Nisman R, Ng C, Vancso GJ (1994) Polym Bull 33:459

180. Vancso GJ, Nisman R, Snétivy D, Schönherr H, Smith P, Ng C, Yang H (1994) Coll Surf A 87:263
181. Sills S, Overney RM, Gotsmann B, Frommer J (2005) Tribol Lett 19:9
182. Urbakh M, Klafter J, Gourdon D, Israelachvili J (2004) Nature 430:525